ELSEVIER

Contents lists available at ScienceDirect

#### International Journal of Pharmaceutics

journal homepage: www.elsevier.com/locate/ijpharm





### Effect of shape on the physical properties of pharmaceutical tablets

Tipu Sultan <sup>a</sup>, Xiaochi Xu <sup>a</sup>, Enamul Hasan Rozin <sup>a</sup>, Joona Sorjonen <sup>b</sup>, Jarkko Ketolainen <sup>b</sup>, Håkan Wikström <sup>c</sup>, Luis Martin de Juan <sup>d</sup>, Pirjo Tajarobi <sup>c</sup>, Cetin Cetinkaya <sup>a,\*</sup>

- a Photo-Acoustics Research Laboratory, Department of Mechanical and Aerospace Engineering, Clarkson University, Potsdam, NY 13699-5725, USA
- <sup>b</sup> School of Pharmacy, Faculty of Health Sciences, University of Eastern Finland, Kuopio, Finland
- <sup>c</sup> Early Product Development and Manufacturing, Pharmaceutical Sciences, BioPharmaceuticals R&D, AstraZeneca, Gothenburg, Sweden
- <sup>d</sup> Oral Product Development, Pharmaceutical Technology & Development, Operations, AstraZeneca, Gothenburg, Sweden

#### ARTICLE INFO

# Keywords: Physical/mechanical properties of compressed tablets Oral solid dosage forms Tablet geometric shape Ultrasonic characterization techniques Robotic tablet handling Continuous manufacturing

#### ABSTRACT

Despite a well-established process understanding, quality issues for compressed oral solid dosage forms are frequently encountered during various drug product development and production stages. In the current work, a non-destructive contact ultrasonic experimental rig integrated with a collaborative robot arm and an advanced vision system is presented and employed to quantify the effect of the shape of a compressed tablet on its mechanical properties. It is observed that these properties are affected by the tablet geometric shapes and found to be linearly sensitive to the compaction pressures. It is demonstrated that the presented approach significantly improves the repeatability of the experimental waveform acquisition. In addition, with the increased confidence levels in waveform acquisition accuracy and corresponding pressure and shear wave speeds due to improved measurement repeatability, we conclude that pharmaceutical compact materials can indeed have a negative Poisson's ratio, therefore can be auxetic. The presented technique and instrument could find critical applications in continuous tablet manufacturing, and its real-time quality monitoring as measurement repeatability has been significantly improved, minimizing product quality variations.

#### 1. Introduction

The compressed drug tablet is the most popular oral solid dosage form in use worldwide, but compared to many other industries, the equipment and technology currently employed in the pharmaceutical manufacturing industry are often considered outdated (Rantanen and Khinast, 2015). Problems in pharmaceutical tablet design/development and manufacturing have the potential to significantly impact patient care as failures in quality may result in serious harm to patients, costly product recalls, and perilous medicine shortages (CDER, 2017).

Recent advances in technology, design, instrumentation, and software have led to the introduction of several novel techniques for the non-invasive characterization of the physical–mechanical properties of compressed oral solid dosage forms, including near-infrared (NIR) spectroscopy, terahertz pulsed chracterization (Bawuah and Zeitler, 2021), X-ray micro-tomography, Raman spectroscopy, nuclear magnetic resonance (NMR), imagingthermal-based techniques, and laser-induced breakdown spectroscopy, as well as various acoustic techniques (Ketolainen et al., 1995; Leskinen et al., 2010; Simonaho et al., 2011;

Varghese and Cetinkaya, 2007). As reviewed and discussed in detail (Dave et al., 2017), each of these technique has its specific advantages or challenges concerning operational efficiency, practicality, and cost, compared to the traditional analytical methods such as the USP reference standards. It is noteworthy that, currently, a vast majority of these techniques are used as secondary analytical tools to support the traditional methods of characterizing, testing, or monitoring tablet quality attributes. Therefore, further developments in instrumentation (e.g., advanced sensors and automated handling systems) and software (e.g., machine learning models and blockchain technologies) for tablet development, testing, and manufacturing are required to address the emerging needs arising due to new production and business requirements, such a continuous manufacturing, real-time release, and reshoring (FDA, 2020; FDA-2019-D-0298, 2019).

Ultrasonic methods are a class of non-destructive testing techniques based on the propagation and detection of ultrasonic (elastic strain) waves in an object or material tested with the aid of an electromechanical transducer. In its most common applications, a short ultrasonic pulse wave in the range of microseconds is transmitted into and

E-mail address: cetin@clarkson.edu (C. Cetinkaya).

<sup>\*</sup> Corresponding author.

detected from a sample to detect internal defects (irregularities) or to characterize the mechanical properties of materials. Today, a spectrum of ultrasonic testing and characterization techniques includes aircoupled ultrasonic characterization, contact ultrasonic testing, and photo-acoustic methods.

The main advantages of the contact ultrasonic technique in evaluating tablet properties are its measurement speed (on the order of 100 s of microseconds), operational simplicity, and equipment/software cost (Liu and Cetinkaya, 2010). The contact ultrasound method often requires no or minimal sample preparation (Simonaho et al., 2011), and the whole volume of the tablet can be evaluated. In addition, unlike near-infrared (NIR) and THz spectroscopy methods, no model calibration is required in the contact ultrasound method, which makes it fast and easy to adopt (Dave et al., 2017). In Akseli et al. (2008a), a contact ultrasonic method for in-die real-time tablet monitoring system integrated into a compaction punch based on the associated intellectual property (Cetinkaya, 2019, 2017, 2014) was introduced and commercialized (Kern et al., 2022).

An ultrasound scan can be used to measure the time-of-flight (ToF) within the sample, as well as the amplitude of the reflected waves (Akseli et al., 2009). Hakulinen et al., (2008) showed that the velocity of ultrasound waves correlated with the tablet microstructure, e.g., porosity. Akseli et al., (2011) and Simonaho et al., (2011) showed that propagation speed increases with the tensile strength of the sample tablet and thus concluded that propagation speeds measurements are sensitive and a non-destructive means of measuring tablet tensile strengths. Leskinen et al., (2013) and Razavi et al., (2016) found that propagation speed is sensitive to the mixing time of MgSt and the dwell time in tableting. Along with the tensile strength measurements, the ultrasound method has been tested to measure elastic properties such as Young's modulus (Akseli et al., 2010, 2009; Akseli and Cetinkaya, 2008b, 2008a; Ketolainen et al., 1995).

In our reported experiments, two types of material mixtures, four types of tablet geometric shapes, and three target tensile strength levels  $(\sigma)$  were employed. The effects of these experimental parameters on the ultrasonic extracted mechanical properties of the tablets were evaluated, quantified, and reported. We also introduce a novel ultrasonic experimental rig (TOTO experimental set-up) integrated with a collaborative robot arm and an advanced vision system for improving the measurement accuracy and repeatability of the experimentally extracted waveforms and evaluating the effect of the tablet geometric shapes on the mechanical properties of the compacts.

The specific objectives of the reported study include: (i) the analysis of the effects of the tablet geometric shapes on the compact mechanical and ultrasonic properties at a range of compaction pressure levels, (ii) the extraction of the mechanical properties ( $c_L$ ,  $c_T$ ,  $E_A$ , and  $\nu$ ) of the compact materials from acquired acoustic waveforms in an automated, non-destructive manner, and (iii) the demonstration and quantification of the repeatability of the extracted mechanical properties with the TOTO robotic-based experimental set-up.

#### 2. Materials and methods

#### 2.1. Tablet materials and manufacturing

In the current study, two types of the material mixture (referred hereafter to as MCC-DCPA and MCC-MAN) were prepared with the binary mix of (i) Microcrystalline Cellulose (MCC) and Dibasic Calcium Phosphate Anhydrous (DCPA) and (ii) Mannitol (MAN) and Microcrystalline Cellulose (MCC) with the weight percentage ratios of 68.95:29.55 and 68.95:29.55, respectively. Magnesium stearate was added as the lubricant (1.5%).

Microcrystalline cellulose (MCC) is a purified, partially depolymerized alpha-cellulose excipient made by acid hydrolysis of specialty wood (or cotton) pulp. In the current study, Avicel® PH102 (FMC Biopolymer, Cork, Ireland) and Mannitol (PEARLITOL® 100SD,

Roquette, Lestrem, France) are utilized. MCC has attractive dry binding (compressibility) properties, enabling the manufacture of tablets by direct compression. Mannitol is an excipient primarily used as a diluent (10-90% w/w) in pharmaceutical formulations. It is a non-cariogenic and non-acidogenic sugar-free sweetener with exceptional physical and chemical stability and no hygroscopicity (Allen, 2000; Yoshinari et al., 2003). Mannitol (MAN) can also be used in direct-compression tablet applications (Debord et al., 1987; Molokhia et al., 1987), for which the granular and spray-dried forms are available. DCPA is a water-insoluble functional filler for wet granulation and direct compression applications that offers improved flow for all powder mixtures, including poorly flowing APIs and plant extracts. EMCOM-PRESS® (Anhydrous, JRS Pharma, Rosenberg, Germany) is the commercial-grade DCPA utilized in the tablet sample set. DCPA and mannitol are brittle excipients, making them attractive excipients in tableting to combine with a plastic filler such as MCC. A common practice in the pharmaceutical industry is to use two different fillers in the formulation to achieve the desired balance between the plastic and brittle properties.

The true density of the sample tablet compacts was measured using a helium pycnometer (Multi Pycnometer MVP-1, Quanta Chrome, Boynton Beach, USA). The true mass densities of the formulations were then calculated using the weigh fractions and determined to be 1.769 g/cm $^3$  for the MCC-DCPA formulation and 1.480 g/cm $^3$  for the MAN-MCC formulation.

Formulations were blended in a V-blender (non-commercial equipment constructed at the University of Eastern Finland, Kuopio, Finland) for 10 min at 20 rpm. Both formulations were compacted into four geometric shapes (Fig. 1) using a rotatory tablet press (PR 1000, PTK-GB, Seoul, South Korea) at 20 rpm turret speed. Three round tooling sets were used with different cup depth (height), namely, flat (no cup), biconvex (with a cup depth (height) of  $h_c = 0.86$  mm) and dual radius ( $h_c = 1.0$  mm), and one oblong tooling ( $h_c = 1.5$  mm). These uncoated test tablets were chipped in handling (Fig. 1). The compacts were compressed to target tensile strengths of 1.5, 2.0 and 2.5 MPa with a target mass of 400 mg. The resulting eight sample sets are referred to as MCC-DCPA Flat, MCC-DCPA Oblong, MCC-DCPA Dual-radius, MCC-DCPA Biconvex, and MAN-MCC Flat, MAN-MCC Oblong, MAN-MCC Dual-radius, MAN-MCC Biconvex (Table 1).

#### 2.2. Compact sample sets

In Table 1, each measured parameter (p) is represented with respect to its mean,  $p_{\text{mean}}$ , and standard deviation (SD) in the form of  $p_{\text{mean}} \pm$  SD. The relative standard deviations  $(100 \times \text{SD}/p_{\text{mean}})$  are also listed as representing the percentage error. The corresponding fractional error is  $\varepsilon = \text{SD}/p_{\text{mean}}$ . Thus,  $p_{\text{mean}} \pm \text{SD} = p_{\text{mean}} \times (1 \pm \varepsilon)$ .

Three datasets with the corresponding levels of target tensile strengths of  $\sigma = 1.5$ , 2.0 and 2.5 MPa (corresponding compaction pressure levels  $P_c$  are included in Table 1) were utilized for each sample set. Altogether, the complete sample set consisted of 24 (8  $\times$  3) types of experimental tablet samples. For each compaction type, ten compacts were characterized with weight, dimensions, and breaking force while a set of five samples were characterized using the ultrasonic equipment. The compact weight, dimensions, and breaking force, and porosity were measured using a Sotax HT-100 tablet tester (Sotax AG, Aesch, Switzerland) for the round compacts, and a Holland C50 tablet tester (Nottingham, UK) was used for breaking force characterization. The compact density was then calculated using cup depths and volumes from tooling drawings. The calculated compact volumes were verified using a Geopyc 1360 envelope density tester (Norcross, Georgia, USA), indicating that the dual-radius and oblong compacts volumes may be underestimated by up to 5% while the other compacts were within the 2% error of the reference methodology.

The tensile strength ( $\sigma$ ) of the compacts was determined using the following expression:

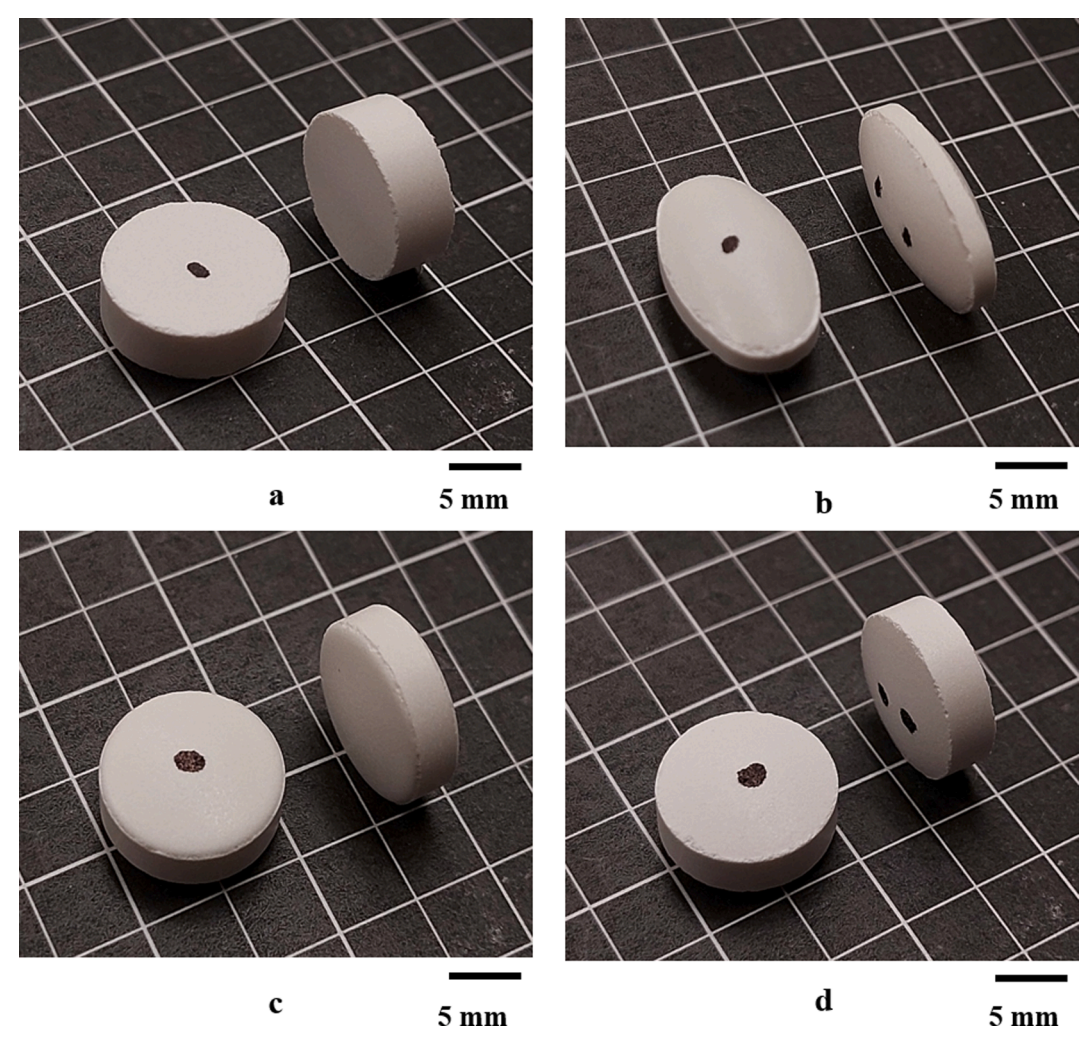


Fig. 1. Images of the utilized compacts with the four geometric shapes of (a) flat, (b) oblong, (c) dual-radius, and (d) biconvex were prepared for the reported ultrasonic evaluation. Background grid: 5 mm by 5 mm.

$$\sigma = \kappa_s \frac{F_B}{\pi l^2} (0.14 \frac{h}{l} + 0.36 \frac{h - 2h_c}{l})^{-1}$$
 (1)

where  $F_{\rm B}$  is the tablet breaking force, l is the characteristic length of the tablet (diameter for round and width for oblong tablets), h is the tablet thickness,  $h_{\rm c}$  is the cup depth (height) of the tooling, and  $\kappa_{\rm s}$  is a shape constant (1 for the round tablets and 2/3 for the oblong tablets) (Pitt and Heasley, 2013; Shang et al., 2013).

#### 2.3. Ultrasonic equipment for waveform acquisition

In the reported experiments, a robotized ultrasonic experimental setup (TOTO System, Pharmacoustics Technologies, LLC, Potsdam, New York, USA) integrated with a data acquisition and analysis software application (Ultrasonic Measurement Instrument (UMI2022), Pharmacoustics Technologies, LLC, Potsdam, New York, USA) was developed and employed to improve the accuracy and the repeatability of the nondestructive ultrasonic evaluation. The TOTO set-up consists of a collaborative robot (UR3e, Universal Robots, Odense S, Denmark) two pressure (compression) transducers (V540-SM, Olympus Corporation, Center Valley, Pennsylvania, USA) with a central frequency of 2.25 MHz, two shear (transverse) wave transducers (V154-RM, Olympus Corporation, Center Valley, Pennsylvania, USA) with a central frequency of 1 MHz, a pair of low attenuation delay-lines. The experimental set-up is controlled by a graphical user interface (GUI-UMI 2022) based on a data acquisition software (LabVIEW 15, National Instruments Corp., Austin, Texas, USA) for signal acquisition and processing, storage, and ToF data analysis (Fig. 2).

The TOTO experimental set-up can be operated in pulse-echo (reflection) or pitch-catch (transmission) modes for both pressure (longitudinal) and shear (transverse) waves. Specifically, the TOTO set-up was employed to acquire the pressure and shear ultrasonic responses of the compacts to characterize their mechanical properties. In the reported pressure and shear experiments, the TOTO set-up operated in pitch-catch mode, and the pulser/receiver parameters were set at a pulse width of 200 ns, pulser voltage of 300 V, a sampling rate of 100 MHz, an amplification gain of 10 dB, and an averaging (oversampling) rate of 512. The pressure and shear transducers were coupled with a delay-line and mounted into Fingertip 01 and Fingertip 02, respectively. The main function of the delay-line integrated into the experimental set-up was to separate the initial acoustic pulse ("main bang") generated by pressure and shear transducers from interface reflections inside the compacts by creating a time-lapse. Receiving pressure and shear transducers were directly mounted into the bottom transducer/sample holder. The transducer/sample holder apparatus holds the compacts securely in place while acquiring waveform and allowing two transducers to approach each other. The robot arm was trained and employed to autonomously center the compacts on the transducer/sample holder while acquiring acoustic waveforms accurately. The transducer/sample holder is supported by a three-point structure-leveling platform that was utilized to calibrate the parallelism of measurement surfaces using a set of adjustment knobs. The robot arm can control the applied axial load

Table 1
The measured average tensile strength  $(\sigma)$ , compact thicknesses (h), apparent mass densities  $(\rho_A)$  are listed along with the acoustically extracted parameters: Time-of-Flight  $(ToF_p \text{ and } ToF_s)$  for pressure and shear waves, pressure and shear wave speeds  $(c_L \text{ and } c_T)$ , the ratio of the pressure and shear speed  $(\kappa)$ , the corresponding Young's moduli  $(E_A)$  and Poisson's ratio  $(\nu)$  with their averages and SDs for the eight sample sets of tablets compressed at the three levels of compaction pressure  $P_c$ .

Sample Set	P <sub>c</sub> (MPa)	Measured Parameters								
		h (mm)	$ ho_{\rm A}$ (kg/m <sup>3</sup> )	ToF <sub>L</sub> (µsec)	ToF <sub>T</sub> (μsec)	c <sub>L</sub> (m/sec)	c <sub>T</sub> (m/sec)	$\kappa (c_{ m L}/c_{ m T})$	E <sub>A</sub> (GPa)	ν
01	48	4.16 ±	$1228.30 \pm 5.40$	5.94 ±	7.09 ±	$701.27 \pm 19.07$	$588.18 \pm 18.41$	1.19 ±	0.60 ±	-0.70 ±
MCC-DCPA		0.03	(0.44%)	0.20	0.26	(2.72%)	(3.13%)	0.02	0.03	0.19
Flat		(0.65%)		(3.30%)	(3.71%)			(2.00%)	(5.60%)	(27.38%)
	71	3.88 ±	$1311.38 \pm 6.03$	$4.12 \pm$	4.82 ±	$940.65 \pm 28.07$	$806.16 \pm 37.09$	$1.17 \pm$	1.16 ±	$-0.97 \pm$
		0.06	(0.46%)	0.16	0.23	(2.98%)	(4.60%)	0.05	0.07	0.42
		(1.44%)		(3.77%)	(4.78%)			(4.04%)	(5.93%)	(43.53%)
	90	3.78 ±	$1357.52 \pm 4.75$	3.74 ±	4.19 ±	1010.84 $\pm$	$901.82 \pm 11.09$	$1.12~\pm$	1.39 ±	$-1.49~\pm$
		0.06	(0.35%)	0.08	0.08	10.17	(1.23%)	0.02	0.02	0.33
		(1.47%)		(2.16%)	(1.85%)	(1.01%)		(1.73%)	(1.78%)	(22.13%)
)2	64	5.05 ±	$1366.86 \pm 9.56$	4.29 ±	6.54 ±	$1175.64~\pm$	$771.44 \pm 7.90$	$1.52 \pm$	$1.89 \pm$	$0.12\pm0.0$
MCC-DCPA		0.02	(0.70%)	0.03	0.05	10.06	(1.02%)	0.01	0.04	(5.15%)
Oblong		(0.33%)	<b>,</b> ,	(0.03%)	(0.81%)	(0.86%)	, ,	(0.47%)	(2.08%)	<b>(</b> )
	85	4.91 ±	$1451.32 \pm 6.82$	$4.02~\pm$	5.88 ±	$1221.34~\pm$	$834.15\pm8.81$	$1.46 \pm$	$2.17~\pm$	$0.06 \pm 0.0$
		0.01	(0.47%)	0.07	0.07	22.56	(1.06%)	0.02	0.09	(29.63%)
		(0.23%)	(	(1.87%)	(1.16%)	(1.85%)	(=====)	(1.13%)	(4.09%)	(======,
	117	4.76 ±	1534.14 $\pm$	3.74 ±	5.46 ±	1271.87 ±	$870.84 \pm 11.27$	1.46 ±	2.48 ±	$0.06 \pm 0.0$
		0.01	13.19	0.05	0.06	18.23	(1.29%)	0.02	0.09	(50.54%)
		(0.24%)	(0.86%)	(1.45%)	(1.11%)	(1.43%)	(1.25,0)	(1.13%)	(3.50%)	(00.0170)
)3	52	4.94 ±	$1309.85 \pm 1.70$	4.19 ±	6.31 ±	1179.24 ±	$781.91 \pm 12.42$	1.51 ±	1.82 ±	$0.11 \pm 0.0$
MCC-DCPA	32	0.01	(0.13%)	0.04	0.10	10.44	(1.59%)	0.02	0.03	(14.66%)
Dual		(0.11%)	(0.1370)	(0.87%)	(1.57%)	(1.19%)	(1.3570)	(1.12%)	(1.79%)	(14.0070)
Radius	74	(0.11%) 4.74 ±	$1376.55 \pm 3.85$	$(0.87\%)$ 3.93 $\pm$	(1.57%) 5.60 ±	$(1.19\%)$ $1206.54 \pm$	$845.18 \pm 8.83$	(1.12%) 1.43 ±	$(1.79\%)$ $2.00 \pm$	$0.02\pm0.0$
radius	7 7	0.01	(0.28%)	0.06	0.05	18.54	(1.04%)	0.02	0.06	(100%)
		(0.12%)	(0.26%)	(1.51%)			(1.04%)	(1.17%)		(100%)
	97	(0.12%) 4.57 ±	1410.01 + 0.06		(0.97%)	(1.54%)	000 06   07 50		(2.95%)	0.04
	9/		$1419.21 \pm 3.26$	3.66 ±	5.09 ±	$1248.51 \pm 7.27$	898.06 ± 27.58	1.39 ±	2.21 ±	$-0.04 \pm 0.06$
		0.04	(0.23%)	0.03	0.13	(0.58%)	(3.07%)	0.03	0.03	0.06
		(0.87%)		(0.83%)	(2.51%)			(2.48%)	(1.35%)	(153.97%
)4	38	5.14 ±	$1186.58 \pm 4.86$	4.97 ±	7.28 ±	1035.38 ±	$705.65 \pm 8.99$	1.47 ±	1.27 ±	$0.06 \pm 0.0$
MCC-DCPA		0.01	(0.41%)	0.15	0.08	30.55	(1.27%)	0.05	0.07	(89.03%)
Biconvex		(0.25%)		(3.05%)	(1.09%)	(2.95%)		(3.61%)	(5.59%)	
	50	$4.93 \pm$	$1247.28 \pm 5.61$	4.49 $\pm$	$6.37~\pm$	$1098.42 \pm 5.09$	$774.44 \pm 10.65$	1.42 $\pm$	$1.50~\pm$	$0.00 \pm 0.0$
		0.01	(0.45%)	0.02	0.08	(0.46%)	(1.38%)	0.02	0.01	(672.05%)
		(0.11%)		(0.55%)	(1.32%)			(1.59%)	(0.67%)	
	70	$4.76 \pm$	$1313.76 \pm 4.47$	4.05 $\pm$	$5.68 \pm$	$1173.20 \pm 7.51$	$838.08 \pm 13.50$	1.40 $\pm$	1.81 $\pm$	$-0.02~\pm$
		0.01	(0.34%)	0.03	0.09	(0.64%)	(1.61%)	0.02	0.03	0.03
		(0.12%)		(0.67%)	(1.50%)			(1.66%)	(1.42%)	(157.06%)
05	52	$4.39 \pm$	1137.80 $\pm$	$3.80 \pm$	$5.00 \pm$	1155.54 $\pm$	$878.90 \pm 21.04$	$1.31~\pm$	$1.52~\pm$	$-0.19~\pm$
MAN-MCC		0.03	35.39	0.13	0.15	34.14	(2.39%)	0.02	0.12	0.04
Flat		(0.68%)	(3.11%)	(3.53%)	(2.99%)	(2.95%)		(1.37%)	(7.96%)	(22.83%)
	76	4.19 $\pm$	$1208.31\pm4.71$	$3.05~\pm$	4.02 $\pm$	1372.15 $\pm$	1042.93 $\pm$	$1.32~\pm$	2.28 $\pm$	$-0.19~\pm$
		0.01	(0.39%)	0.04	0.11	16.93	28.32	0.03	0.06	0.06
		(0.24%)		(1.32%)	(2.85%)	(1.23%)	(2.72%)	(2.08%)	(2.78%)	(34.34%)
	101	$4.07 \pm$	$1244.95 \pm 5.35$	2.74 $\pm$	$3.60 \pm$	1488.65 $\pm$	1133.98 $\pm$	$1.31~\pm$	$2.76 \pm$	$-0.19~\pm$
		0.02	(0.43%)	0.07	0.13	34.51	37.67	0.02	0.14	0.04
		(0.49%)		(2.55%)	(3.51%)	(2.32%)	(3.32%)	(1.19%)	(5.01%)	(20.54%)
06	73	5.26 ±	$1262.01 \pm 4.04$	4.29 ±	6.36 ±	$1227.11~\pm$	$829.73 \pm 39.18$	$1.48 \pm$	1.90 ±	$0.07 \pm 0.0$
MAN-MCC		0.01	(0.32%)	0.04	0.31	10.82	(4.72%)	0.07	0.04	(92.30%)
Oblong		(0.19%)	, ,	(0.87%)	(4.90%)	(0.88%)		(4.70%)	(1.89%)	9
	94	5.13 ±	$1328.01 \pm 9.43$	3.61 ±	5.58 ±	1423.10 ±	$922.61 \pm 68.03$	1.55 ±	2.69 ±	$0.11 \pm 0.3$
		0.05	(0.71%)	0.13	0.41	45.39	(7.37%)	0.17	0.17	(111.73%)
		(0.97%)	"	(3.58%)	(7.26%)	(3.19%)	***************************************	(10.82%)	(6.44%)	
	121	5.07 ±	1405.62 $\pm$	3.50 ±	4.91 ±	$1449.15 \pm 9.28$	1031.98 $\pm$	1.40 ±	2.95 ±	$-0.02~\pm$
		0.02	87.42	0.03	0.08	(0.64%)	16.98	0.03	0.22	0.04
		(0.39%)	(6.22%)	(0.90%)	(1.54%)	(0.0 1.0)	(1.65%)	(1.82%)	(7.48%)	(244.37%
)7	70	(0.39%) 5.14 ±	$1244.83 \pm 5.10$	3.74 ±	$5.33 \pm$	1373.57 $\pm$	$965.20 \pm 11.31$	$1.42 \pm$	2.35 ±	$0.01 \pm 0.0$
MAN-MCC	70	0.01	(0.41%)	0.05	0.06	17.38	(1.17%)	0.02	2.33 ± 0.06	(190.74%)
Dual		(0.19%)	(0.71 /0)	(0.05%)	(1.19%)	(1.27%)	(1.17/0)	(1.10%)	(2.60%)	(130.74%)
Dual Radius	95	(0.19%) 4.96 ±	$1285.39 \pm 2.96$	3.38 ±	$(1.19\%)$ $4.74 \pm$	1466.97 ±	$1046.88 \pm 9.05$	1.40 ±	$(2.00\%)$ $2.77 \pm$	$-0.02~\pm$
	93									
		0.01	(0.23%)	0.03	0.04	10.78	(0.86%)	0.02	0.04	0.02
	107	(0.20%)	1000.00 + 0.00	(0.03%)	(0.91%)	(0.74%)	1110.70	(1.15%)	(1.37%)	(125.76%)
	127	4.83 ±	$1333.22 \pm 3.33$	3.17 ±	4.32 ±	1524.47 ±	1119.72 ±	1.36 ±	3.10 ±	$-0.11 \pm 0.10$
		0.01	(0.25%)	0.04	0.18	18.60	50.81	0.07	0.07	0.18
_		(0.21%)		(1.24%)	(4.24%)	(1.22%)	(4.54%)	(5.30%)	(2.24%)	(166.83%
08	51	5.22 $\pm$	$1159.44 \pm 3.25$	$3.69 \pm$	5.81 $\pm$	1414.38 $\pm$	$898.99 \pm 20.41$	$1.57~\pm$	2.32 $\pm$	$0.16 \pm 0.0$
MAN-MCC		0.04	(0.28%)	0.14	0.10	61.40	(2.27%)	0.03	0.21	(15.57%)
Biconvex		(0.77%)		(3.75%)	(1.73%)	(4.34%)		(2.35%)	(9.19%)	
	89	4.85 $\pm$	$1232.70 \pm 3.57$	3.14 $\pm$	4.66 $\pm$	1544.48 $\pm$	1040.92 $\pm$	1.48 $\pm$	2.94 $\pm$	$0.08\pm0.0$
				0.04	0.07	00.00	15 10	0.00	0.00	(05.000/)
		0.01	(0.29%)	0.04	0.07	23.39	15.12	0.03	0.09	(35.39%)

(continued on next page)

Table 1 (continued)

Sample Set	P <sub>c</sub> (MPa)	Measured Parameters								
		h (mm)	$\rho_{\rm A}$ (kg/m <sup>3</sup> )	ToF <sub>L</sub> (µsec)	ToF <sub>T</sub> (μsec)	c <sub>L</sub> (m/sec)	$c_{\mathrm{T}}$ (m/sec)	$\kappa \ (c_{ m L}/c_{ m T})$	E <sub>A</sub> (GPa)	ν
		$4.68 \pm \\ 0.01 \\ (0.01\%)$	$1294.16 \pm 2.72 \\ (0.21\%)$	$\begin{array}{c} 2.81 \pm \\ 0.02 \\ (0.89\%) \end{array}$	$4.01 \pm \\ 0.09 \\ (2.20\%)$	$1663.69 \pm \\15.57 \\ (0.94\%)$	$1165.89 \pm 26.53 \\ (2.28\%)$	$\begin{array}{c} 1.43 \pm \\ 0.02 \\ (1.38\%) \end{array}$	$3.58 \pm 0.07$ (2.03%)	$0.02 \pm 0.03 \\ (163.29\%)$

(on the sample) during waveform acquisition to eliminate the effects of near-surface asperities on waveform quality without causing damage to the compact. The surface contact force between a transducer and a compact is optimized for the transmission of traveling pulses. During current waveform acquisitions, the applied axial load was maintained at 25 N for ensuring repeatable transmission contact between the compact and the surfaces of the delay-line and transducer. Compared to the compaction pressure  $P_c$  levels (48 – 129 MPa), the exerted axial force (on the order of a few Newton) are extremely low; thus no substantial elastic/plastic effects on compact mechanical integrity and microstructure is expected. The applied axial load can be varied from the robot control program.

Compacts are first placed on the backlight source manually in the reported acoustic pressure and shear transmission experiments in the pitch-catch mode. The spot vision system acquires the sample image over the backlight source to extract the features (e.g., position, orientation, and minor axis length of a compact). Using this information from the spot vision system, collaborative robot gripped sample sorted by xaxis placed on the backlight source and put the compact on the center of the transducer/sample holder autonomously that the bottom surface of the compact contacted with receiving transducer properly. Fingertip 01 housing the pulser out pressure transducer and delayline was vertically placed and centered in contact with the top surface of the compact automatically by the robot and exerted a constant axial load during measurements defined before the experiment in the collaborative robot. An electrical pulse generated by the ultrasonic instrument first excites the pitching pressure transducer. The pressure (longitudinal) wave pulse is transmitted through the delayline, and the compact is placed on the surface of the receiving pressure transducer. Finally, the ultrasonic pulse is sensed by the receiving pressure transducer. The received pulse containing the ToF information was acquired, digitized, signal-processed, and saved as a digital waveform data file via the UMI2022 GUI interface. Once the data acquisition was complete, the robot gripped the sample and placed it in a storage container. This autonomous data acquisition process continued until the last sample was present on the backlight source. The same procedure was implemented for the shear data acquisition using the shear transducers.

#### 2.4. Analysis methods

The acquired pressure (longitudinal) and shear (transverse) waveforms are processed to obtain  $ToF_L$  and  $ToF_T$  determined by the Short-Term Fourier Transform (STFT) time–frequency techniques. In extracting  $ToF_L$  and  $ToF_T$  in a dispersive material, a time–frequency method is employed, which requires the ToF of strain energy at a particular frequency (not necessarily the amplitude of incoming wave pulses) (Drai et al., 2002). For a tablet with a thickness of h, the corresponding average pressure and shear wave speeds ( $c_L$  and  $c_T$ ) are calculated as:

$$c_{\rm L} = h/{\rm ToF_L} \ c_{\rm T} = h/{\rm ToF_T} \tag{2}$$

By assuming one-dimensional wave propagation, the apparent Young's modulus of the material is determined by  $E_{\rm A}=c_{\rm L}^2\times\rho_{\rm A}$ , where  $\rho_{\rm A}$  is the apparent mass density of the sample material. For an isotropic material, the Poisson's ratio ( $\nu$ ) as a function of the wave speed ratio  $\kappa=c_{\rm L}$  /  $c_{\rm T}$  is given by.

$$\nu(\kappa) = \frac{1}{2} \left( \frac{\kappa^2 - 2}{\kappa^2 - 1} \right) \tag{3}$$

#### 3. Results and discussions

In line with USP Reference Standard < 1062> (for tablet mechanical strength characterization), Fig. 3.a shows the relationship between compaction pressure ( $P_c$ ) and porosity ( $\phi^m$ ) (measured or re-calculated depending on the tablet type) for the four tablet shapes of the two formulations. These are referred to as the compressibility profile. Additionally, in Fig. 3.b, the relationship between compaction pressure ( $P_c$ ) and measured tensile strength ( $\sigma^m$ ) for the four tablet shapes of the two formulations, referred to as the tabletability profile, is shown.

As the envelope density measurements indicated that the drawings of tooling used for the dual radius and oblong compacts might include error, the original porosity value was re-calculated by increasing the compact volume for these shapes by 5% to compensate for this measurement inaccuracy for dual radius and oblong tablets. As expected, the compressibility profile (Fig. 3.a) is the same regardless of the compact shape but note that the formulation has a significant influence.

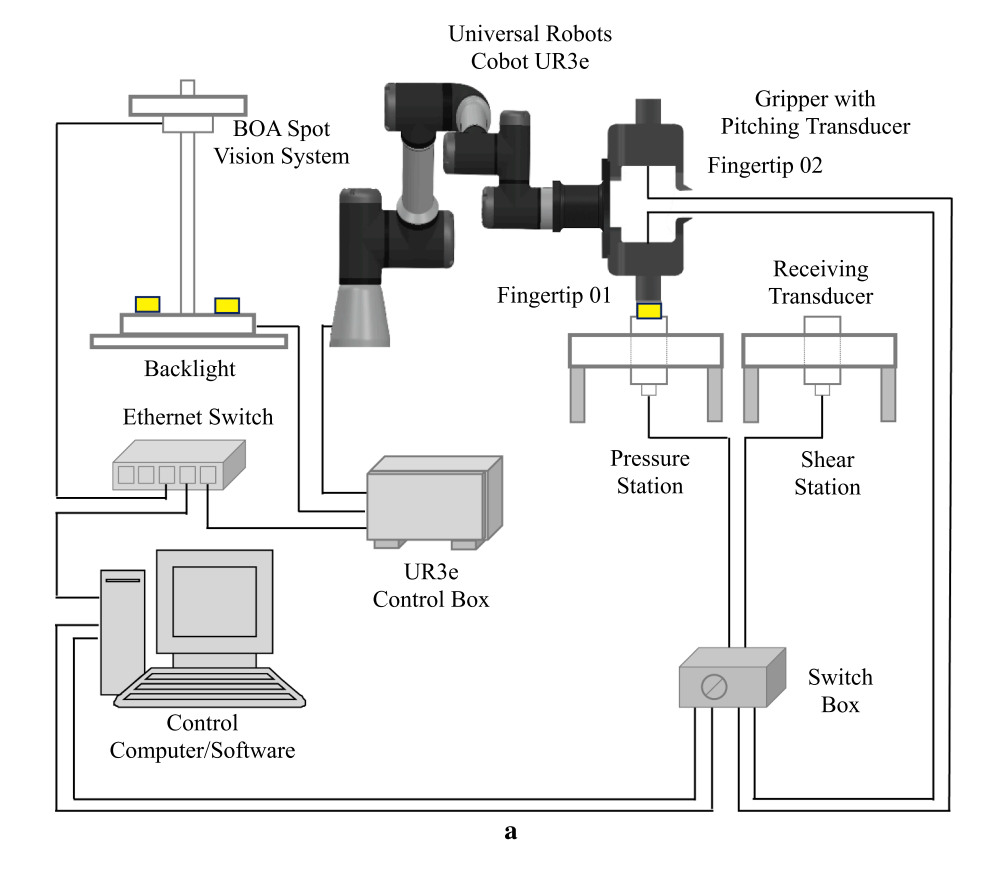
As it is evident from Fig. 3.b, there is only a very slight difference for shapes with different formulations in tabletability between the different compact shapes of the same formulation except for the oblong shape. This observation supports the findings of Yohannes and Abebe (2021) that currently adapted equations for determining the tensile strength of oblong compacts are overly simplified to be considered highly accurate.

In Fig. 4, the normalized pressure and shear waveforms for the MCC-DCPA and MAN-MCC sample sets with four tablet geometric shapes (flat, oblong, dual-radius and biconvex) with the delay line waveform (dotted) at the corresponding compaction pressure ( $P_1 = 1.5 \text{ MPa}$ ,  $P_2 = 2.0 \text{ MPa}$ , and  $P_3 = 2.5 \text{ MPa}$ ) are depicted. In the pressure waveforms for the MCC-DCPA sample set in Fig. 4.a, it is observed that the arrival times of pressure pulses shorten with the increasing compaction pressure (from  $P_1$  to  $P_3$ ), indicating the ToF is sensitive to the compaction pressure  $P_c$ . The shifting trend was less evident at higher compaction pressure levels ( $P_2$  and  $P_3$ ). In addition, the arrival times of pressure pulses vary for each sample set with pressure level ( $P_1$  to  $P_3$ ), indicating tablet shape types affect the pressure wave propagation speed.

In Fig. 4.b, a similar trend is observed for the sample MAN-MCC sets. This trend is also observed for shear waveforms (Fig. 4.c-d). It is noted that the pressure and shear ToFs are sensitive to the compaction pressure, and the tablet shape affects the arrival of pressure and shear pulses, which indicates the compaction force and tablet shape modify the pressure and shear wave speed (Fig. 4).

In Table 1, the measured average compact thicknesses (h), apparent mass densities ( $\rho_A$ ) and the acoustically extracted parameters: pressure and shear ToFs (ToF<sub>L</sub> and ToF<sub>T</sub>, respectively), pressure and shear wave speeds ( $c_L$  and  $c_T$ ), the ratio of the pressure and shear speed ( $\kappa$ ), corresponding Young's moduli ( $E_A$ ) and Poisson's ratio ( $\nu$ ) for the three levels of compaction pressure ( $P_1=1.5$  MPa,  $P_2=2.0$  MPa, and  $P_3=2.5$  MPa) are summarized for the sample sets.

As seen in Fig. 4, the arrival of the pressure and shear pulses are shifted to the left with the increasing compaction pressure (from  $P_1$  to  $P_3$ ), indicating a reduction in the  $ToF_L$  and  $ToF_T$  values. The pressure wave ToF values for the tablet sample set MCC-DCPA Flat were obtained as  $ToF_L = 5.94$ , 4.12, and  $3.74\mu sec$  for each  $P_c$  level, respectively (Fig. 4. a), which indicates that  $ToF_L$  and  $ToF_T$  are sensitive to the compaction pressure. In Fig. 4, it is also observed that the pressure and shear pulse arrival times differ between the sample sets with varying tablet geometric shapes at each  $P_c$  level (implying a change in speeds), i.e.,  $ToF_L$ 



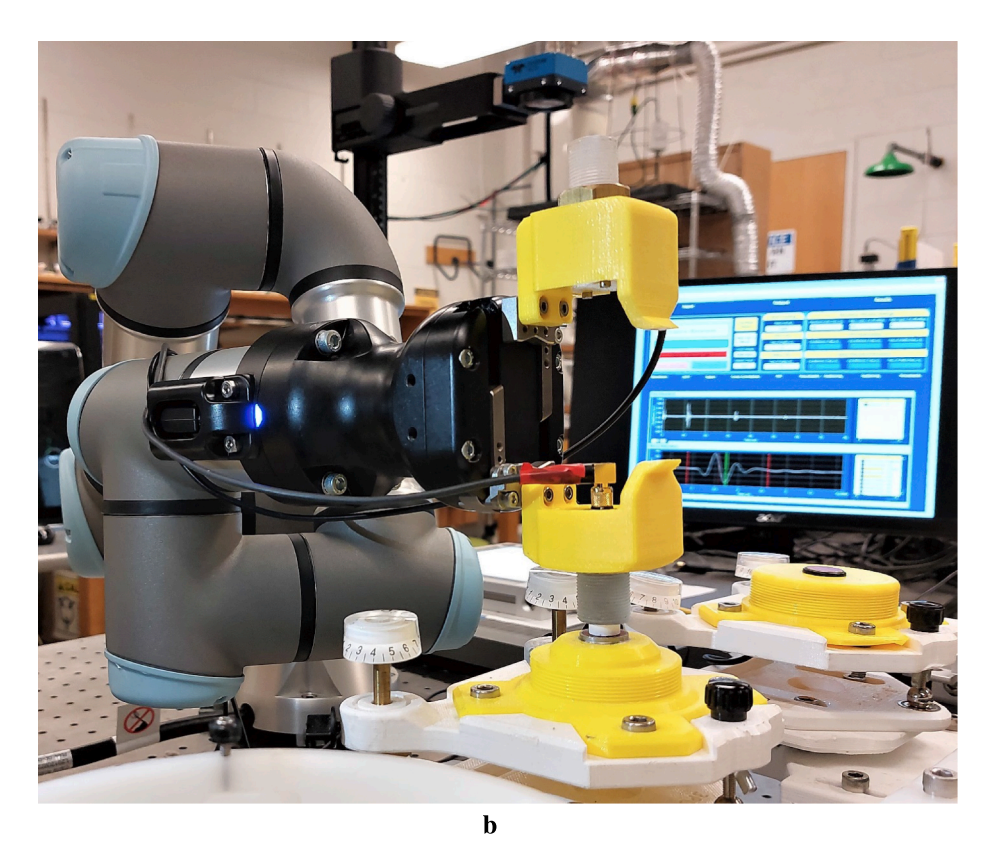


**Fig. 2.** (a) Connectivity diagram of the experimental rig (TOTO experimental set-up) consisting of a BOA Spot vision system for locating the sample position, a collaborative robot as the sample handling system, a cobot gripper integrated with the pulsing pressure and shear transducers for sample picking and ultrasonic testing, and the receiving pressure and shear transducer holders for operating the system in the pitch-catch mode. (b) Image of the TOTO experimental set-up.

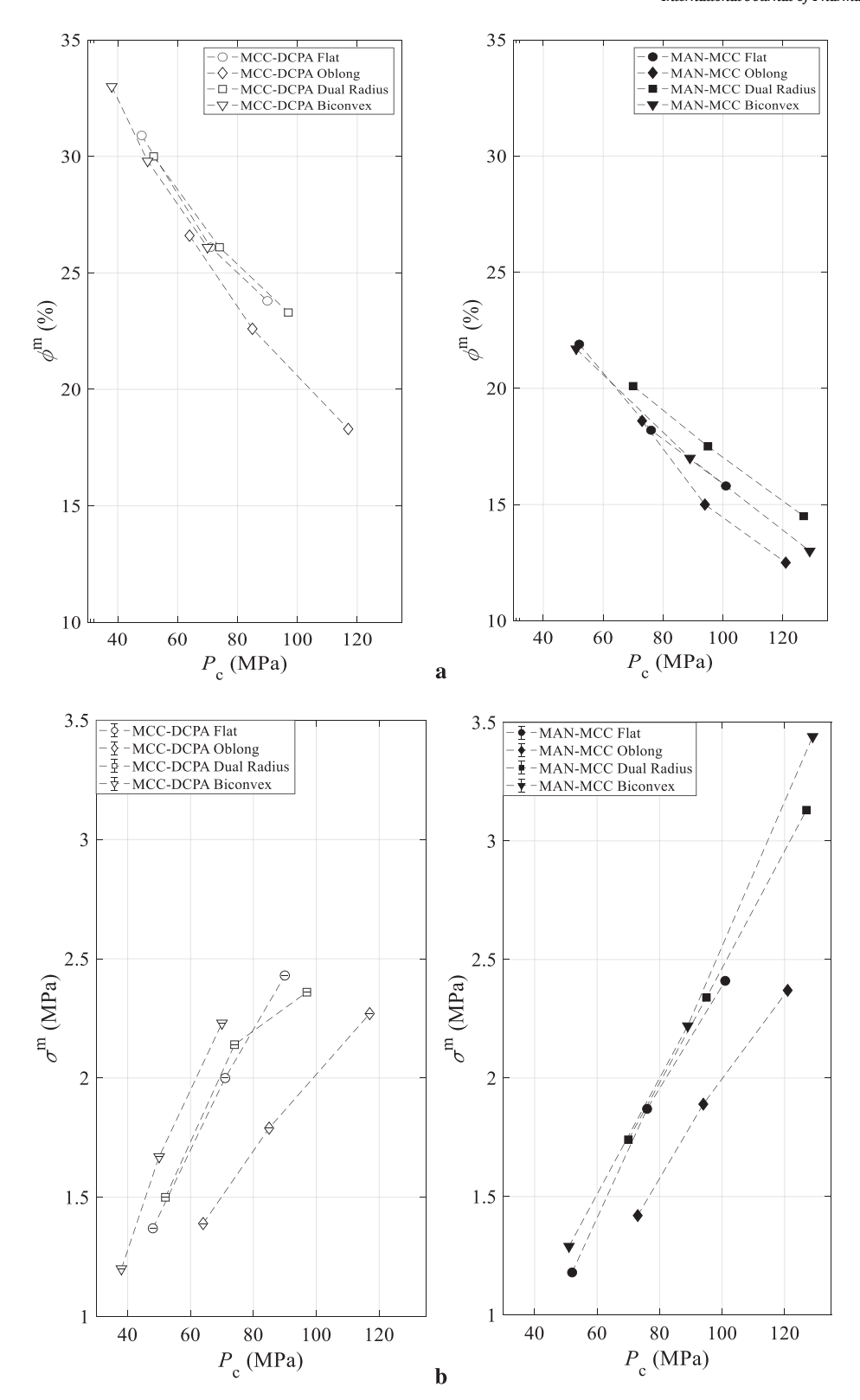


Fig. 3. Relationship between compaction pressure ( $P_c$ ) and directly measured (a) porosity ( $\phi^m$ ) (tabletability plot) and (b) tensile strength ( $\sigma^m$ ) (compressibility plot) for the MCC-DCPA (left) and MAN-MCC (right) sample sets with the four tablet shapes.

5.94, 4.29, 4.19, and 4.97 $\mu$ sec (Fig. 4.a) at compaction level  $P_1$ , respectively. It is indicated that the types of tablet geometric shapes modulated the ToF.

Superimposed plots for  $\rho_A$ ,  $c_L$ ,  $c_T$ , and  $E_A$  with a function of compaction pressure  $P_c$  for each tablet shape are presented in Fig. 4. It is observed that the  $\rho_A$ ,  $c_L$ ,  $c_T$ , and  $E_A$  curves for all sample sets increase

with increasing compaction pressures  $(P_1-P_3)$ , indicating pressure and shear wave speeds  $(c_{\rm L}$  and  $c_{\rm T})$  were strongly modulated by  $P_{\rm c}$ . It is also seen that  $\rho_{\rm A}$ ,  $c_{\rm L}$ ,  $c_{\rm T}$ , and  $E_{\rm A}$  values vary between the tablet shapes at each  $P_{\rm c}$ .

First we quantify the effect of the tablet shape on the speed of pressure (longitudinal) waves  $(c_L)$  in the MCC-DCPA and MAN-MCC

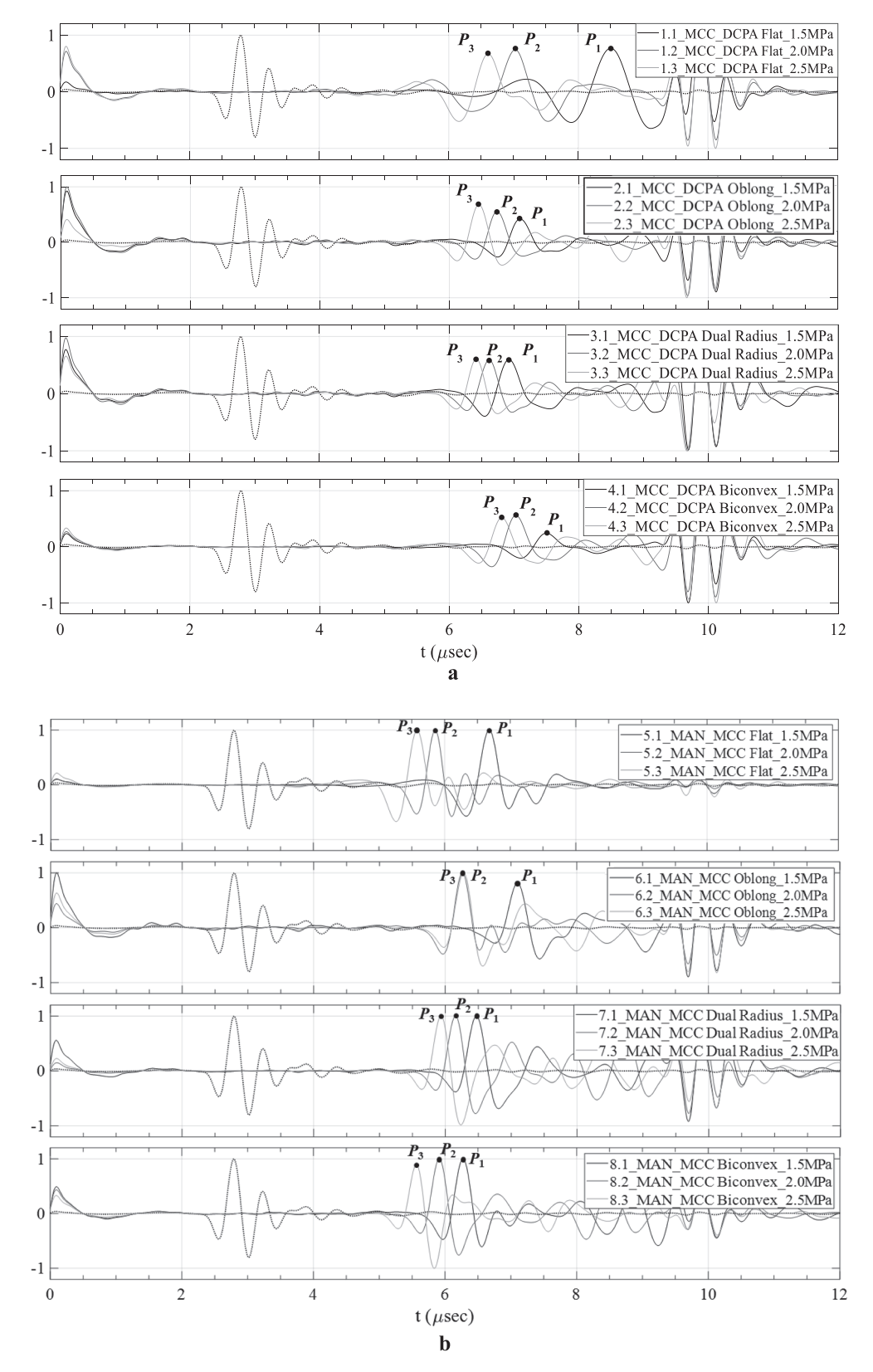


**Fig. 4.** Normalized pressure (*a-b*) and shear (*c-d*) waveforms for the MCC-DCPA and MAN-MCC sample sets with the four tablet shapes (as shown in the legends) with the delay line waveform (dotted) at the corresponding compaction pressures.

sample sets. In Fig. 5.a, for the MCC-DCPA sample set, it is observed that at  $P_1$ ,  $c_{\rm L}^{\rm dr}$  is 1.39% greater than the pressure wave speed  $c_{\rm L}^{\rm ob}$ ,  $c_{\rm L}^{\rm ob}$  is 11.44% larger than  $c_{\rm L}^{\rm bc}$ , and  $c_{\rm L}^{\rm bc}$  is 56.81% larger than  $c_{\rm L}^{\rm flat}$  ( $c_{\rm L}^{\rm dr}$   $_{\rm C}$   $c_{\rm L}^{\rm ob}$   $_{\rm C}$   $c_{\rm L}^{\rm ob}$ 

 $c_{\rm L}^{\rm flat}),$  while compaction pressure levels changes from  $P_2$  to  $P_3,$   $c_{\rm L}^{\rm ob}$  is 1.37 and 2.18% larger than  $c_{\rm L}^{\rm dr},$   $c_{\rm L}^{\rm dr}$  is 6.44 and 4.91% larger than  $c_{\rm L}^{\rm bc},$  and  $c_{\rm L}^{\rm bc}$  is 17.45 and 16.62% larger than  $c_{\rm L}^{\rm flat}$  ( $c_{\rm L}^{\rm ob} > c_{\rm L}^{\rm dr} > c_{\rm L}^{\rm flat})$ . In the same way,

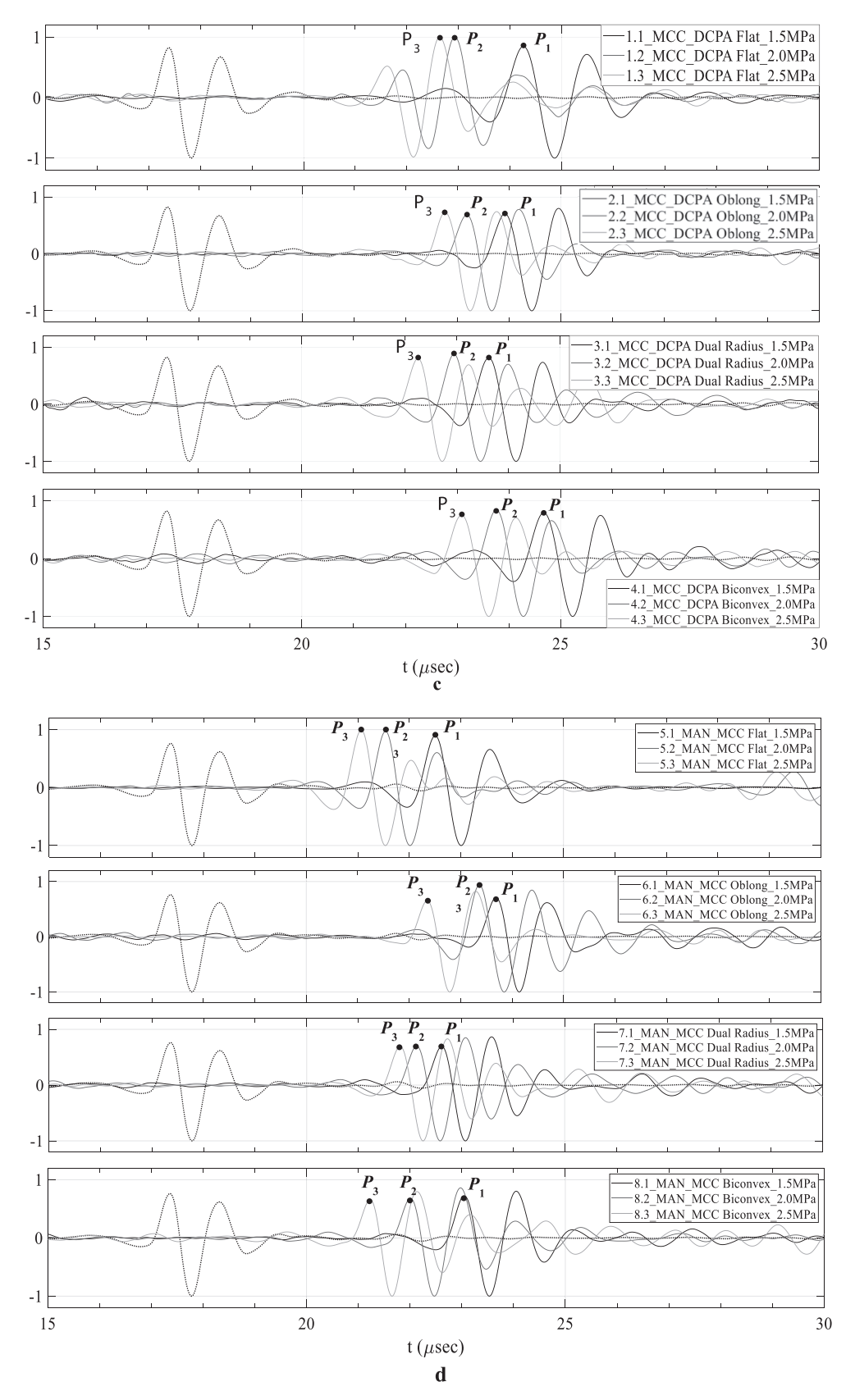
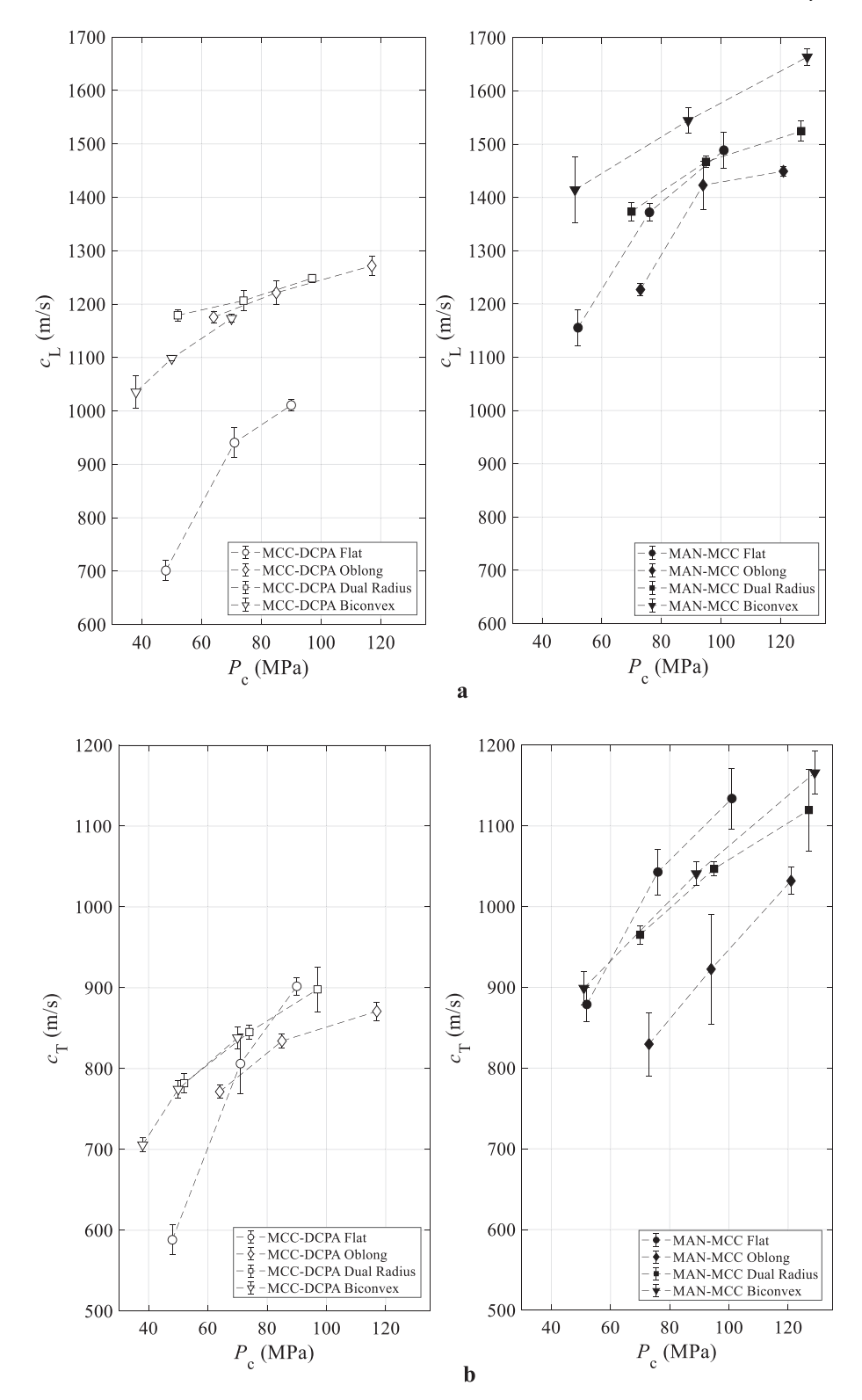


Fig. 4. (continued).

for the MAN-MCC sample set, from  $P_1$  to  $P_2$ , the pressure speed  $c_{\rm L}^{\rm bc}$  is 2.15 and 4.54% greater than  $c_{\rm L}^{\rm dr}$ ,  $c_{\rm L}^{\rm dr}$  is 13.47 and 2.43% larger than  $c_{\rm L}^{\rm ob}$ , and  $c_{\rm L}^{\rm ob}$  is 4.23 and 2.56% larger than  $c_{\rm L}^{\rm flat}$  ( $c_{\rm L}^{\rm bc} > c_{\rm L}^{\rm dr} > c_{\rm L}^{\rm ob} c_{\rm L}^{\rm flat}$ ), while at  $P_3$ ,

 $c_{\rm L}^{\rm ob}$  is 18.70% greater than  $c_{\rm L}^{\rm bc}$ ,  $c_{\rm L}^{\rm bc}$  is 4.79% larger than  $c_{\rm L}^{\rm flat}$ , and  $c_{\rm L}^{\rm flat}$  is 2.11% larger than  $c_{\rm L}^{\rm dr}$  ( $c_{\rm L}^{\rm ob}$  >  $c_{\rm L}^{\rm bc}$  >  $c_{\rm L}^{\rm flat}$   $c_{\rm L}^{\rm dr}$ ).

Similarly, the effect of the tablet shape on the speed of shear



**Fig. 5.** Relationship between  $P_c$  and (a) pressure wave speeds ( $c_L$ ), (b) shear wave speeds ( $c_T$ ), (c) apparent densities ( $\rho_A$ ), (d) apparent Young's modulus ( $E_A$ ) and (e) Poisson's ratio ( $\nu$ ) for the MCC-DCPA (*left*) and MAN-MCC (*right*) sample sets with the four tablet shapes.

(transverse) waves  $(c_T)$  in the samples is also investigated and quantified. In Fig. 5.b, for the MCC-DCPA sample set, the transverse wave speed  $c_T^{\rm dr}$  is 0.79% greater than  $c_T^{\rm ob}$ ,  $c_T^{\rm ob}$  is 9.87% larger than  $c_T^{\rm bc}$ , and  $c_T^{\rm bc}$  is 21.52% larger than  $c_T^{\rm flat}$  at  $P_1$  ( $c_T^{\rm dr} > c_T^{\rm ob} > c_T^{\rm bc}$   $c_T^{\rm flat}$ ), and at  $P_2$   $c_T^{\rm dr}$  is 1.23% greater than  $c_T^{\rm ob}$ ,  $c_T^{\rm ob}$  is 5.97% larger than  $c_T^{\rm flat}$ , and  $c_T^{\rm flat}$  is 1.18% larger

than  $c_{\rm T}^{\rm bc}$  ( $c_{\rm T}^{\rm dr}>c_{\rm T}^{\rm ob}>c_{\rm E}^{\rm flat}$   $c_{\rm T}^{\rm bc}$ ), and at  $P_3$   $c_{\rm T}^{\rm flat}$  is 0.34% greater than  $c_{\rm T}^{\rm dr}$ ,  $c_{\rm T}^{\rm dr}$  is 3.14% larger than  $c_{\rm T}^{\rm ob}$ , and  $c_{\rm T}^{\rm ob}$  is 4.63% larger than  $c_{\rm T}^{\rm bc}$  ( $c_{\rm T}^{\rm flat}>c_{\rm T}^{\rm cd}>c_{\rm E}^{\rm dr}>c_{\rm E}^{\rm ob}$ ). For the MAN-MCC sample set,  $c_{\rm T}^{\rm dr}$  is 7.34% larger than  $c_{\rm T}^{\rm bc}$ ,  $c_{\rm T}^{\rm bc}$  is 2.43% larger than  $c_{\rm T}^{\rm flat}$ , and  $c_{\rm T}^{\rm flat}$  is 4.59% larger than  $c_{\rm T}^{\rm ob}$  at  $P_1$  ( $c_{\rm T}^{\rm dr}>c_{\rm T}^{\rm bc}>c_{\rm T}^{\rm flat}>c_{\rm T}^{\rm$ 

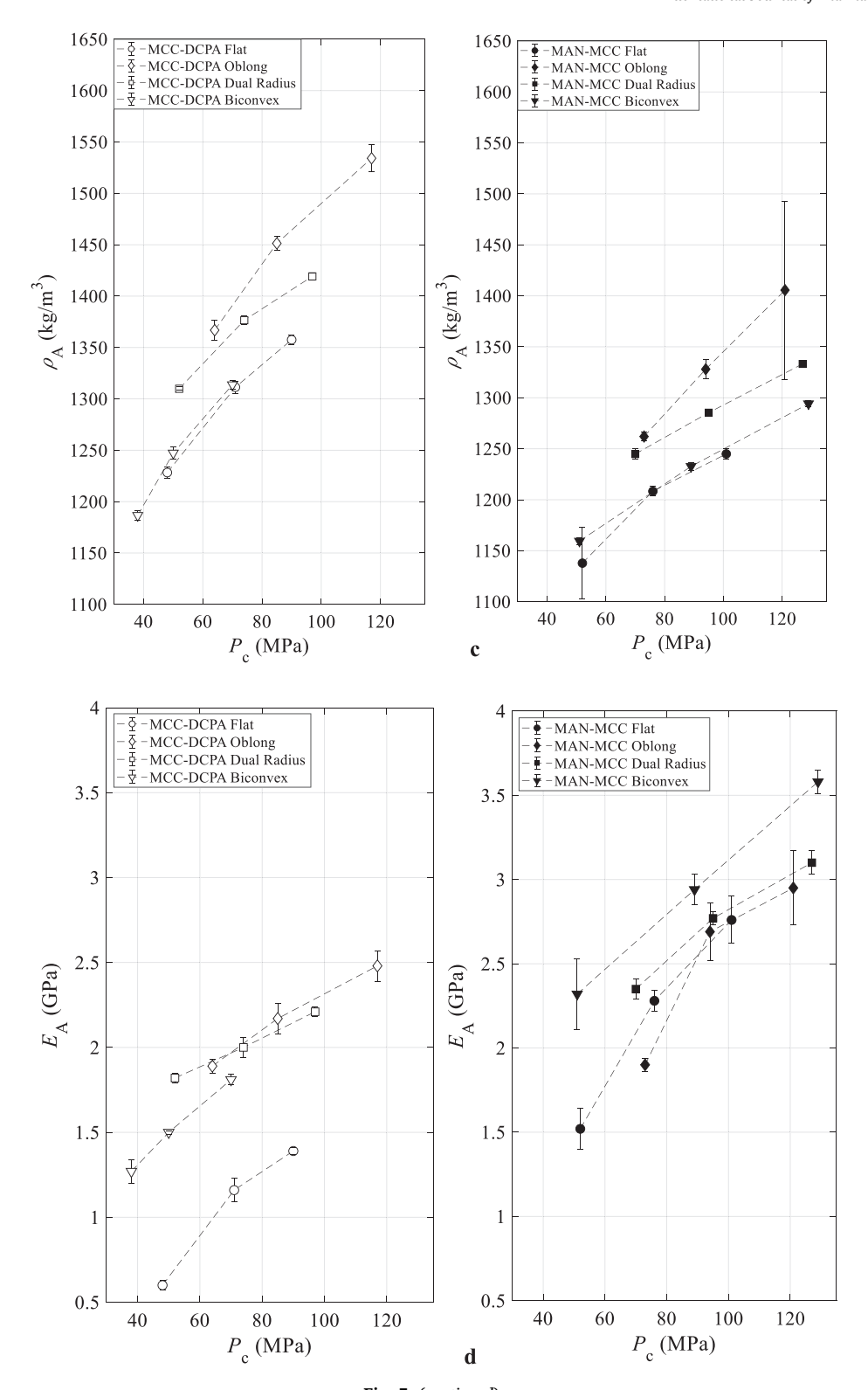


Fig. 5. (continued).

8.95% larger than  $c_{\rm T}^{\rm ob}$  at  $P_2$  ( $c_{\rm T}^{\rm flat} > c_{\rm T}^{\rm dr} > c_{\rm T}^{\rm bc}$   $c_{\rm T}^{\rm ob}$ ), and  $c_{\rm T}^{\rm flat}$  is 1.13% larger than  $c_{\rm T}^{\rm bc}$ ,  $c_{\rm T}^{\rm bc}$  is 6.76% larger than  $c_{\rm T}^{\rm dr}$ ,  $c_{\rm T}^{\rm dr}$  is 7.36% larger than  $c_{\rm T}^{\rm ob}$  at  $P_3$  ( $c_{\rm T}^{\rm flat} > c_{\rm T}^{\rm bc} > c_{\rm T}^{\rm dc} > c_{\rm T}^{\rm ob}$ ).

In Fig. 5.c, the effect of the tablet shape on the apparent mass density ( $\rho$ ) in the samples is demonstrated and quantified. Note that, for the MCC-DCPA sample set from  $P_1$  to  $P_3$ , the apparent mass density of the oblong tablets  $\rho_{\rm ob}$  is 4.35, 5.45, and 8.10% greater than the apparent mass density of the dual-radius tablets  $\rho_{\rm dr}$ ,  $\rho_{\rm dr}$  is 6.59, 4.96, and 4.57%

greater than the apparent density of the flat tablets  $\rho_{flat}$ , and  $\rho_{flat}$  is 3.54, 5.13, and 3.27% greater than the apparent density of the biconvex tablet  $\rho_{bc}$  ( $\rho_{ob} > \rho_{dr} > \rho_{flat} > \rho_{bc}$ ). For the MAN-MCC sample set, from  $P_1$  to  $P_3$ ,  $\rho_{ob}$  is 1.45, 3.35, and 5.40% greater than  $\rho_{dr}$ ,  $\rho_{dr}$  is 7.33, 4.30, and 3.01% greater than  $\rho_{bc}$ , and  $\rho_{bc}$  is 1.93, 1.99, and 3.94% greater than  $\rho_{flat}$  ( $\rho_{ob} > \rho_{dr} > \rho_{bc} > \rho_{flat}$ ), respectively.

The effect of the tablet shape on the apparent Young's modulus ( $E_A$ ) in the samples is shown in Fig. 5.d. From  $P_1$  to  $P_3$ , for the MCC-DCPA

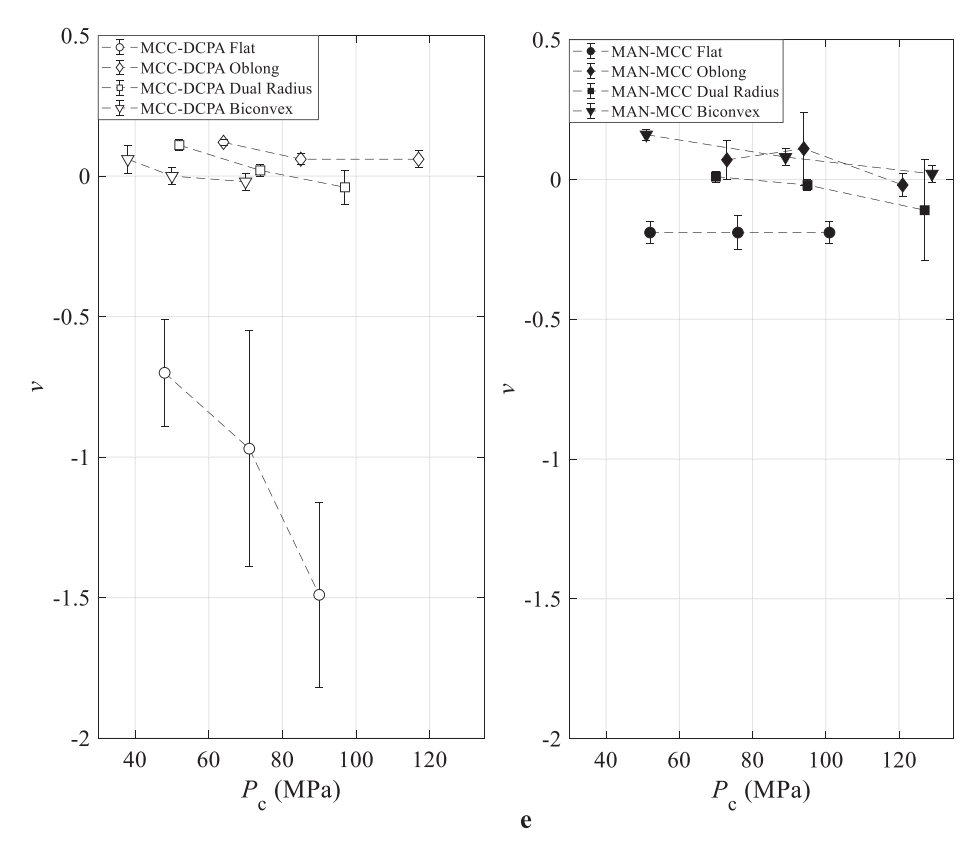


Fig. 5. (continued).

sample set,  $E_A^{ob}$  is 1.50, 8.53, and 12.88% greater than  $E_A^{dr}$ ,  $E_A^{dr}$  is 40.85, 24.85, and 18.88% larger than  $E_A^{bc}$ , and  $E_A^{bc}$  is 136.67, 31.01, and 31.54% larger than  $E_A^{flat}$  ( $E_A^{ob} > E_A^{dr} > E_A^{bc} > E_A^{flat}$ ). For the MAN-MCC sample set,  $E_A^{dr}$  is 2.53% larger than  $E_A^{bc}$ ,  $E_A^{bc}$  is 23.44% larger than  $E_A^{ob}$ , and  $E_A^{ob}$  is 20.75% larger than  $E_A^{flat}$  at  $P_1$  ( $E_A^{fr} > E_A^{fr} > E_A^{fr} > E_A^{flat}$ ),  $E_A^{flat}$  is 4.63% larger than  $E_A^{flat}$  at  $P_1$  ( $E_A^{fr} > E_A^{fr} > E_A^{flat} > E_A^{flat} > E_A^{fr} > E_A^{fr$ 

Based on these observations, summarized in Fig. 5, it is concluded that the material parameters  $\rho_{A}$ ,  $c_{L}$ ,  $c_{T}$ , and  $E_{A}$  correlate well with the compaction pressure level  $P_{C}$  and the effect of the tablet shapes on the mechanical properties of the sample tablet sets are determined and quantified.

The values of Poisson's ratio v, determined by the extracted  $c_{\rm L}$  and  $c_{\rm T}$  from Eq. 2 for all the sample sets at each compaction pressure level, are listed in Table 1. In Fig. 5.e, for all sample sets (except MAN-MCC Flat and Oblong), it is observed that Poisson's ratio v decreased with the increase in  $P_{\rm c}$  (from  $P_{\rm 1}$  to  $P_{\rm 3}$ ) (i.e., for MAN-MCC Biconvex sample set, Poisson's ratio v values of 0.16, 0.08, and 0.02 from  $P_{\rm 1}$  to  $P_{\rm 3}$ ). No such trend was observed for the other sample sets. The accuracy of  $\kappa$  determination can be increased by using higher frequency transducers and advanced time–frequency signal processing techniques.

## 3.1. Correlation of the compact porosity and tensile strength with the ultrasonically extracted propagation speeds and Young's modulus

The relations between the measured porosity  $\phi^m$ , tensile strengths  $\sigma^m$  and the pressure, shear velocities, and Young's modulus of the compacts  $(c_L, c_T, \text{ and } E_A)$  for the eight sample sets at three levels of compaction pressure  $(P_1, P_2, \text{ and } P_3)$  are depicted in Fig. 6. It is observed that, for all sample sets, the pressure and shear velocities and Young's modulus  $(c_L, c_T, \text{ and } E_A)$  decrease with increasing the porosity  $\phi^m$  and increase with increasing the compact tensile strength $\sigma^m$ . This observation indicates that  $c_L, c_T, \text{ and } E_A$  values are found to correlate with the measured  $\phi^m$ 

and  $\sigma^{\text{m}}$  (Fig. 6). In addition,  $c_{\text{L}}$ ,  $c_{\text{T}}$ , and  $E_{\text{A}}$  curves are distinct and separated from sample sets at each compaction pressure level and found to reflect the effect of tablet geometric shapes on the mechanical properties ( $c_{\text{L}}$ ,  $c_{\text{T}}$ , and  $E_{\text{A}}$ ).

#### 3.2. Measurement precision and error analysis

In Fig. 7.a, Poisson's ratio (Eq. 2) is plotted as a function of the speed ratio  $\kappa = c_{\rm L}/c_{\rm T}$ , indicating the increased measurement errors in low values of  $\kappa$  as the slope of the  $\nu(\kappa)$  curve increases for low  $\kappa$  values (e.g. 1.4-1.7). To quantify the error sensitivity, a first-order error perturbation analysis is performed by relating the perturbation level errors in the  $ToF_L$  and  $ToF_T$  to the resultant errors in the Poisson's ratio  $\nu$  evaluations. More specifically, ToF<sub>L</sub> and ToF<sub>T</sub> are perturbed as ToF<sub>L</sub>  $\rightarrow$  To F<sup>o</sup><sub>L</sub> (1 +  $\varepsilon_L$ ) and  $ToF_T \rightarrow To F_T^0$  (1 +  $\varepsilon_T$ ), here  $\varepsilon$  is taken as fractional measurement error of a wave ToF, and the effects of extracted quantities are determined as a function of  $\varepsilon$ . For example, if the measurement error is 10%, the corresponding fractional error is  $\varepsilon = 0.1$ . Determining the corresponding error in the Poisson's ratio  $\nu$  value is particularly of practical interest due to the fact that Poisson's ratio characterization is often a challenging task. If the resulting Poisson's ratio is expressed as perturbed  $\nu$  (1 +  $\Delta\nu$ ), the task is to determine the fractional resultant error  $\Delta \nu$  as a function of the fractional measurement error  $\varepsilon$ . By perturbing ToF<sub>L</sub> and ToF<sub>T</sub> with fractional errors ( $\varepsilon_L$ ,  $\varepsilon_T$ ) with respect to their average values as given below:

$$c_L = h/(1 + \varepsilon_L) ToF_L^o \ c_T = h/(1 + \varepsilon_T) ToF_T^o$$
(4)

with.

$$c_L^o=h/{\it ToF_L^o}c_T^o=h/{\it ToF_T^o}\kappa^o=rac{c_L^o}{c_T^o}=rac{{\it ToF_T^o}}{{\it ToF_L^o}}$$

a relationship  $\Delta \nu = f(\varepsilon_L, \, \varepsilon_T)$  from the Taylor series expansion of Eq. (3) with the perturbation analysis conducted in the ToF<sub>L</sub> and ToF<sub>T</sub> measurements and their fractional errors, the Taylor series expansion for  $\nu(\kappa)$  with higher-order terms becomes:

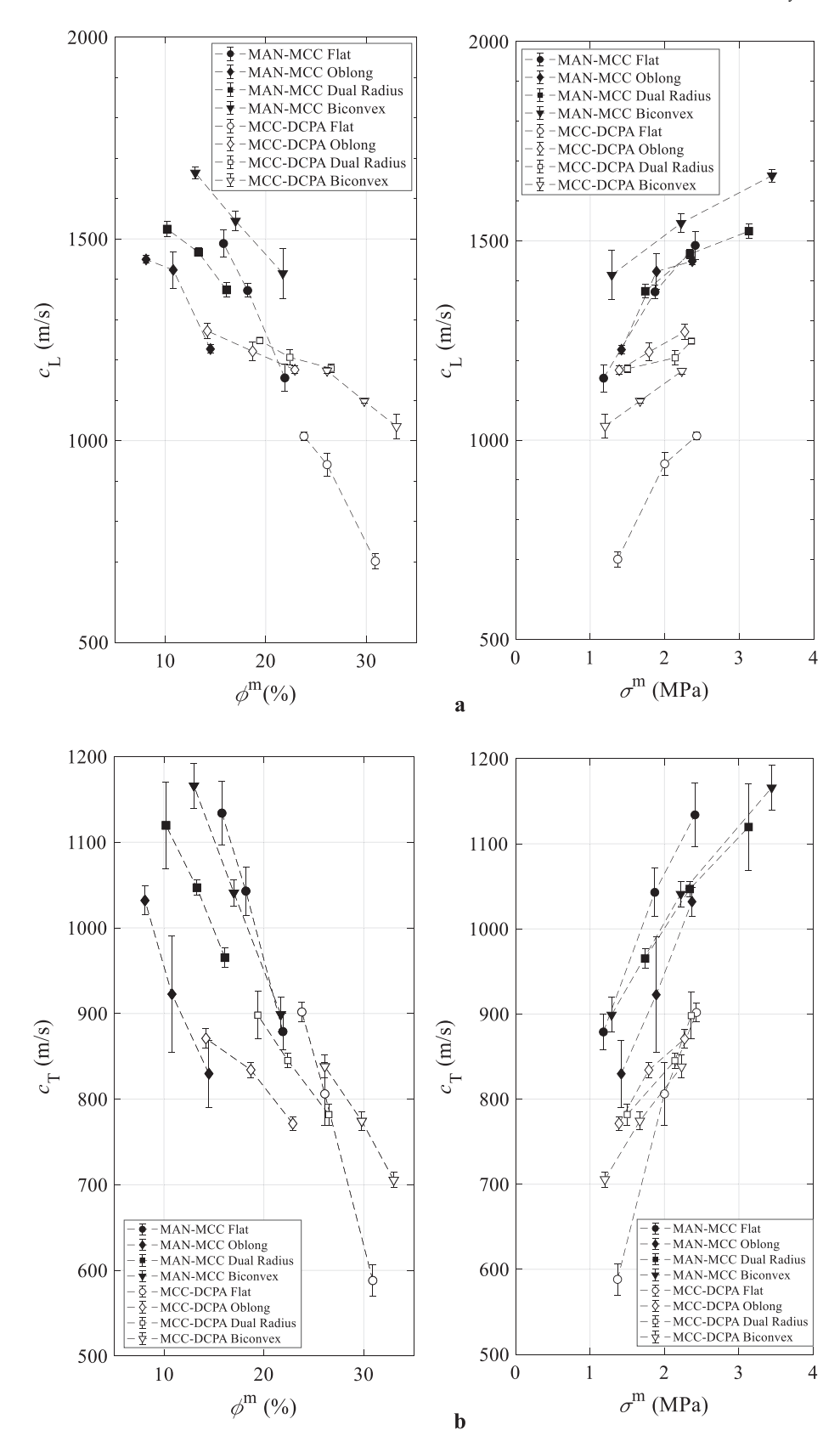


Fig. 6. Relationships between the measured  $\phi^{\rm m}$  (left) and  $\sigma^{\rm m}$  (right) and acoustically extracted mechanical properties: (a)  $c_{\rm L}$ , (b)  $c_{\rm T}$ , and (c)  $E_{\rm A}$  for the sample sets.

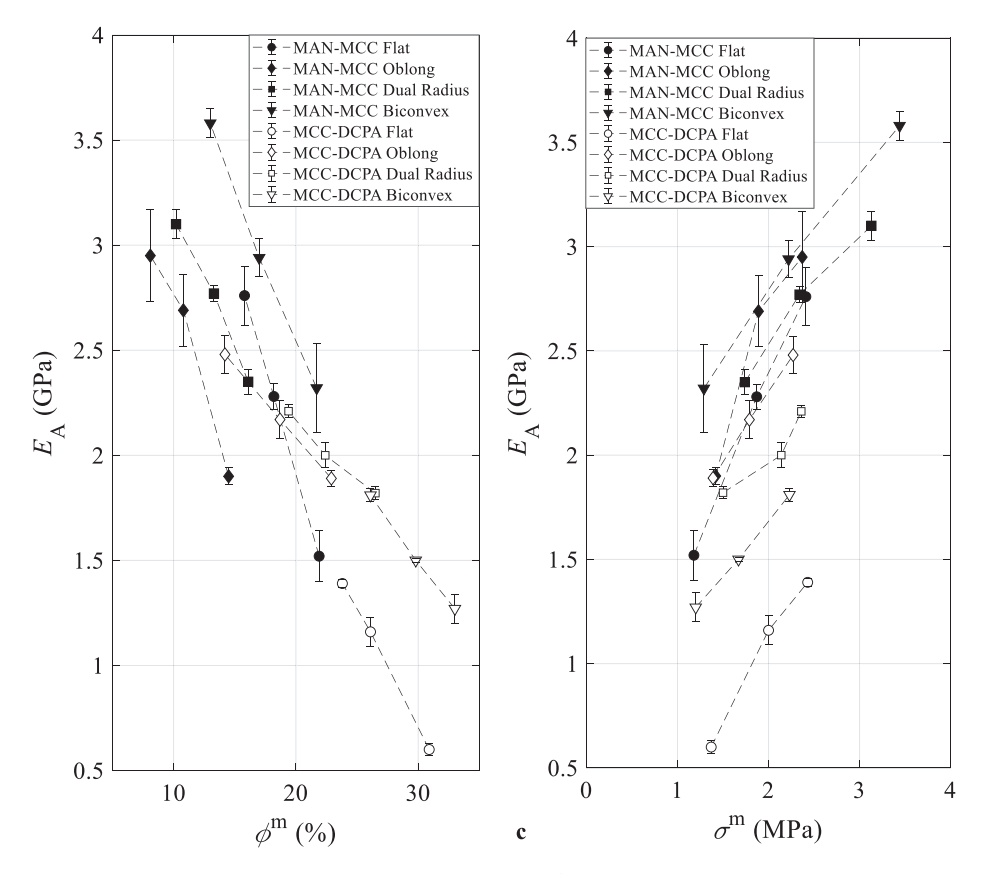


Fig. 6. (continued).

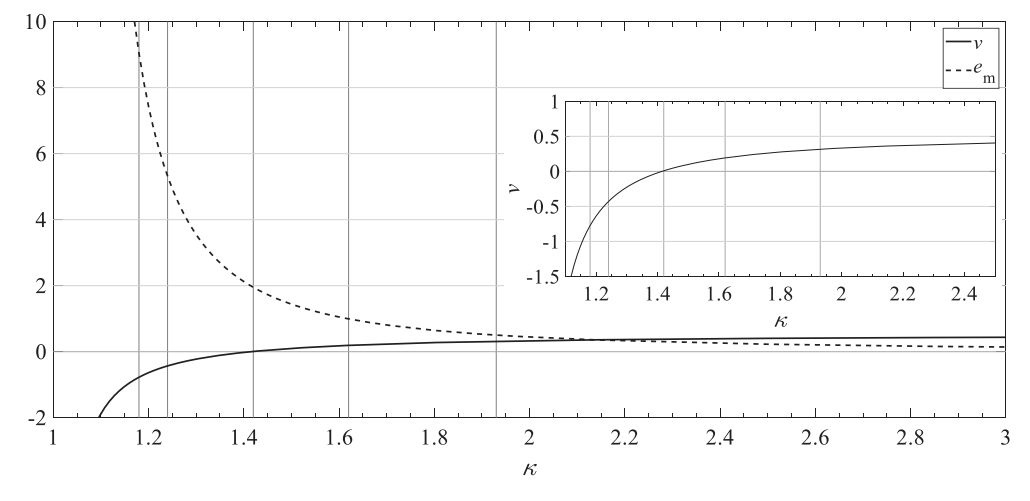


Fig. 7.  $\kappa$  (ultrasonic speed ratio) versus  $\nu$  (Poisson's ratio) and the error magnification factor  $e_{\rm m}$ . Inset: Close-up of  $\kappa$  versus  $\nu$ . The vertical lines correspond to the error magnification factors of  $e_{\rm m}=10,\,5,\,2,\,1,\,1/2$  (from left to right, respectively).

$$\nu(\kappa) = \frac{1}{2} \left( \frac{\left( (1 + \varepsilon_T) To F_T^o / (1 + \varepsilon_L) To F_L^o \right)^2 - 2}{\left( (1 + \varepsilon_T) To F_T^o / (1 + \varepsilon_L) To F_L^o \right)^2 - 1} \right) = \nu(\kappa^o) + \left( \frac{To F_L^o}{\left( To F_L^o \right)^2 - \left( To F_T^o \right)^2} \right)^2 (\varepsilon_T - \varepsilon_L) + O(.)$$

$$= \nu(\kappa^o) + e_m(\varepsilon_T - \varepsilon_L) + O(.)$$
(5)

where O(.) stands for higher-order terms in the expansion,  $e_{\rm m}$  the error magnification factor in the extraction of the Poisson's ratio  $\nu(\kappa)$  from the speed ratio  $\kappa$ , and  $(\varepsilon_{\rm L}, \, \varepsilon_{\rm T})$  the fractional error factors in the ultrasonic pressure (L) and shear (T) wave speed measurements, respectively.  $e_{\rm m}$  in Eq. (5) is determined as follows:

$$e_{m}(\kappa^{o}) = \left(\frac{ToF_{L}^{o} \ ToF_{T}^{o}}{\left(ToF_{L}^{o}\right)^{2} - \left(ToF_{T}^{o}\right)^{2}}\right)^{2} = \frac{\left(\kappa^{o}\right)^{2}}{\left(\left(\kappa^{o}\right)^{2} - 1\right)^{2}} = \frac{1}{\left(\kappa^{o} - \frac{1}{\kappa^{o}}\right)^{2}} = \frac{d\nu(\kappa^{o})}{d\kappa^{o}}\kappa^{o}$$
(6)

with

$$\frac{d\nu(\kappa)}{d\kappa} = \frac{\kappa}{(\kappa^2 - 1)^2}$$

The first-order measurement error in the extracted Poisson's ratio value  $\nu(\kappa)$  is approximated as  $e_{\rm m}(\varepsilon_{\rm L}\text{-}\varepsilon_{\rm T})$  as obtained from the first-order term of its Taylor series expansion (Eq. (6)). In Fig. 7,  $\nu(\kappa)$  and  $e_{\rm m}$  are shown as a function of  $\kappa$ . For low values  $\kappa$ , the  $\nu(\kappa)$  curve is steeper, indicating error amplification. The values of  $e_m$  for  $\kappa = 10, 5, 2, 1, \frac{1}{2}$  are depicted by vertical lines in Fig. 5, indicating substantial error amplification, e.g., a factor of 10 at  $\kappa = 1.17$  ( $\nu = -0.85$ ), and a factor of 5 at  $\kappa$ = 1.248 (v = -0.40). Materials with a negative Poisson's ratio, also known as auxetic materials, exhibit unusual and counterintuitive mechanical behavior. For example, an auxetic cylindrical sample becomes thinner in cross-section when compressed and larger when it is in tension. The results reported here, coupled with the above perturbation analysis, indicate that the materials of pharmaceutical compacts can be auxetic. To our best knowledge, no systematic characterization/imaging study on the local arrangement of powder particles and micro-scale residual stresses eliminating the possibility negative Poisson's ratio in compressed OSDs has been reported. In a compressed OSD material with multiple constituents, it is theoretically possible that the micro-scale arrangement of powder particles and porosity and the equilibrium of local (residual) stress/strain state could occur such a manner that its resulting mechanical/physical properties would exhibit auxetic mechanical response.

#### 4. Conclusions and remarks

In the current study, a design space of four tablet geometric shapes (flat, oblong, dual radius, and biconvex), with three targeted tensile strength levels ( $\sigma_1=1.5$  MPa,  $\sigma_2=2.0$  MPa, and  $\sigma_3=2.5$  MPa), and two compact material mixture types (MCC-DCPA and MAN-MCC) is introduced. The effect of tablet shape and formulations on compact mechanical (physical) properties was evaluated. The mechanical properties of the tablets ( $c_L$ ,  $c_T$ ,  $E_A$ , and  $\nu$ ) were non-destructively extracted based on the ultrasonic waveform, and the measured mechanical properties of the compacts show high repeatability (with low SDs). The reported properties were found to be linearly sensitive to the compaction pressure, and their dependency on the tablet geometric shapes was clearly observed and quantified. The Poisson's ratio  $\nu$  values determined by  $\kappa$  had a decreasing trend in the sample set MCC-DCPA Oblong, MCC-DCPA Dual Radius, and MCC-DCPA Biconvex.

Based on the extracted ToF (ToF<sub>L</sub> and ToF<sub>T</sub>) results of the pressure and shear wave propagation in the reported tablets, the apparent mass density  $\rho_A$ , the pressure and shear wave speeds ( $c_L$  and  $c_T$ ), Young's modulus ( $E_A$ ) and Poisson's ratio ( $\nu$ ) of the compact materials were determined and reported. It was noted that  $\rho_A$ ,  $c_L$ ,  $c_T$ , and  $E_A$  values increased with increasing  $P_c$ , indicating that the mechanical properties ( $\rho_A$ ,  $c_L$ ,  $c_T$ , and  $E_A$ ) and compaction pressure  $P_c$  are in correlation. Note that  $E_A$  was increasing faster than  $\rho_A$ , indicating that  $E_A$  was dominated by the pressure wave speed  $c_L$ . In addition,  $\rho_A$ ,  $c_L$ ,  $c_T$ ,  $E_A$  values vary between tablet geometric shapes (i.e., flat, oblong, dual radius, and biconvex) at each  $P_c$ , it is concluded that tablet geometric shapes affect the mechanical properties of the compacts. Moreover,  $c_L$ ,  $c_T$  and  $E_A$  curves for the sample set MAN-MCC were higher than MCC-DCPA at

each  $P_{\rm c}$ . In comparison, the apparent mass density  $\rho_{\rm A}$  for the sample MAN-MCC was lower than MCC-DCPA, indicating that the differences in the mechanical properties of materials can be detected using reported ultrasonic experimental methods. In sum, the mechanical properties ( $\rho_{\rm A}$ ,  $c_{\rm L}$ ,  $c_{\rm T}$  and  $E_{\rm A}$ ) of the tablets were found to be sensitive to the compression pressure, tablet geometric shapes, and changes in compact material mixture pair.

The analysis of the experimental data indicates that the ultrasonic extracted pressure and shear wave velocities and Young's modulus ( $c_{\rm L}$ ,  $c_{\rm T}$ , and  $E_{\rm A}$ ) correlated with the directly measured porosity and tensile strength ( $\phi^m$  and  $\sigma^m$ ) for all the sample sets.

The presented methodology can be adopted at various materials processing research, tablet design, product development, and solid dosage production stages. The results reported in Fig. 5 can be used by a tablet designer in taking the shape of a tablet (along with compaction pressure) into consideration when predicting its tensile strength. In addition, with the increased confidence level in waveform acquisition and corresponding pressure and shear wave speeds due to improved measurement repeatability in the robotic TOTO system, we conclude that pharmaceutical compact materials can indeed have a negative Poisson's ratio known as auxetic materials. Previously negative Poisson's ratio measurements for compacts were often attributed to measurement errors since the sensitivity of Poisson's ratio measurements in low  $c_{\rm I}/c_{\rm T}$  ranges is low.

#### CRediT authorship contribution statement

Tipu Sultan: Formal analysis, Investigation, Visualization, Writing – review & editing. Xiaochi Xu: Formal analysis, Investigation, Visualization, Writing – review & editing. Enamul Hasan Rozin: Formal analysis, Investigation, Visualization, Writing – review & editing. Joona Sorjonen: Investigation. Jarkko Ketolainen: Supervision, Writing – review & editing. Håkan Wikström: Methodology, Writing – review & editing. Luis Martin de Juan: Methodology, Pirjo Tajarobi: Supervision, Writing – review & editing. Cetin Cetinkaya: Conceptualization, Methodology, Software, Data curation, Writing – original draft, Supervision.

#### **Declaration of Competing Interest**

The authors declare that they have no known competing financial interests or personal relationships that could have appeared to influence the work reported in this paper.

#### Data availability

No data was used for the research described in the article.

#### Acknowledgements

Authors acknowledge funding from NSF STTR grant (Awards Number: 2051895) and AstraZeneca for providing tableting materials and formulations. Authors would like to thank Peter Jonsson (AZ) for the physical characterization of tablets, Sara Fennvik (AZ) for the GeoPyc measurements, and Prof. Ossi Korhonen (University of Eastern Finland) for help in tableting and sample preparation, and Pharmacoustics Technologies, LLC (Potsdam, New York, USA) for providing the ultrasonic instrument and software utilized in the reported experiments.

#### References

Akseli, I., Becker, D.C., Cetinkaya, C., 2009. Ultrasonic determination of Young's moduli of the coat and core materials of a drug tablet. Int. J. Pharm. 370 (1-2), 17–25. https://doi.org/10.1016/j.ijpharm.2008.11.003.

Akseli, I., Cetinkaya, C., 2008a. Drug tablet thickness estimations using air-coupled acoustics. Int. J. Pharm. 351 (1-2), 165–173. https://doi.org/10.1016/j. ijpharm.2007.09.036.

- Akseli, I., Cetinkaya, C., 2008b. Air-coupled non-contact mechanical property determination of drug tablets. Int. J. Pharm. 359 (1-2), 25–34. https://doi.org/ 10.1016/j.ijpharm.2008.03.020.
- Akseli, I., Libordi, C., Cetinkaya, C., 2008. Real-time Acoustic Elastic Property Monitoring of Compacts During Compaction. J Pharm Innov 3 (2), 134–140. https://doi.org/10.1007/s12247-008-9029-z.
- Akseli, I., Dey, D., Cetinkaya, C., 2010. Mechanical Property Characterization of Bilayered Tablets using Nondestructive Air-Coupled Acoustics. AAPS PharmSciTech 11 (1), 90–102. https://doi.org/10.1208/s12249-009-9352-9.
- Akseli, I., Iyer, S., Lee, H.P., Cuitiño, A.M., 2011. A Quantitative Correlation of the Effect of Density Distributions in Roller-Compacted Ribbons on the Mechanical Properties of Tablets Using Ultrasonics and X-ray Tomography. AAPS PharmSciTech 12 (3), 834–853. https://doi.org/10.1208/s12249-011-9640-z.
- Allen, L.V., 2000. Featured excipient: capsule and tablet diluents. Int. J. Pharm. Compd. 4, 306–312.
- Bawuah, P., Zeitler, J.A., 2021. Advances in terahertz time-domain spectroscopy of pharmaceutical solids: A review. TrAC, Trends Anal. Chem. 139, 116272. https:// doi.org/10.1016/j.trac.2021.116272.
- CDER, 2017. Advancement of Emerging Technology Applications for Pharmaceutical Innovation and Modernization. https://www.fda.gov/files/drugs/published/Advancement-of-Emerging-Technology-Applications-for-Pharmaceutical-Innovation-and-Modernization-Guidance-for-Industry.pdf.
- Cetinkaya, C., 2014. Non-contact mechanical property determination of drug tablets. US8645084B1.
- Cetinkaya, C., 2017. Methods and systems for in-and out-of-die monitoring and characterization of multi-component tablets and for detecting and monitoring stiction and tooling material modifications on punch and die surfaces. US9739753B2.
- Cetinkaya, C., 2019. Methods and systems for in-and out-of-die monitoring and characterization of multi-component tablets and for detecting and monitoring stiction and tooling material modifications on punch and die surfaces. US10429352B2.
- Dave, V.S., Shahin, H.I., Youngren-Ortiz, S.R., Chougule, M.B., Haware, R.V., 2017. Emerging technologies for the non-invasive characterization of physical-mechanical properties of tablets. Int. J. Pharm. 532 (1), 299–312. https://doi.org/10.1016/j. iipharm.2017.09.009.
- Debord, B., Lefebvre, C., Guyot-Hermann, A.M., Hubert, J., Bouché, R., Cuyot, J.C., 1987. Study of different crystalline forms of mannitol: comparative behaviour under compression. Drug Dev. Ind. Pharm. 13 (9-11), 1533–1546.
- Drai, R., Khelil, M., Benchaala, A., 2002. Time frequency and wavelet transform applied to selected problems in ultrasonics NDE. NDT and E Int. 35 (8), 567–572. https://doi.org/10.1016/S0963-8695(02)00041-5.
- FDA-2019-D-0298, 2019. Quality Considerations for Continuous Manufacturing. https://www.fda.gov/regulatory-information/search-fda-guidance-documents/quality-considerations-continuous-manufacturing.

- FDA, 2020. Drug Shortages for Calendar Year 2020. https://www.fda.gov/media/ 150409/download.
- Hakulinen, M.A., Pajander, J., Leskinen, J., Ketolainen, J., van Veen, B., Niinimäki, K., Pirskanen, K., Poso, A., Lappalainen, R., 2008. Ultrasound Transmission Technique as a Potential Tool for Physical Evaluation of Monolithic Matrix Tablets. AAPS PharmSciTech 9 (1), 267–273. https://doi.org/10.1208/s12249-007-9010-z.
- Kern, M., Riedel, T., Breitkreutz, J., 2022. Investigating key properties of model excipients and binary powder blends using ultrasonic in-die measurements on a compaction simulator. Int. J. Pharm. 613, 121381. https://doi.org/10.1016/j. ijpharm.2021.121381.
- Ketolainen, J., Oksanen, M., Rantala, J., Stor-Pellinen, J., Luukkala, M., Paronen, P., 1995. Photoacoustic evaluation of elasticity and integrity of pharmaceutical tablets. Int. J. Pharm. 125 (1), 45–53. https://doi.org/10.1016/0378-5173(95)00110-5.
- Leskinen, J.T.T., Simonaho, S.-P., Hakulinen, M., Ketolainen, J., 2010. In-line ultrasound measurement system for detecting tablet integrity. Int. J. Pharm. 400 (1-2), 104–113. https://doi.org/10.1016/j.ijpharm.2010.08.038.
- Leskinen, J.T.T., Simonaho, S.-P., Hakulinen, M., Ketolainen, J., 2013. Real-time tablet formation monitoring with ultrasound measurements in eccentric single station tablet press. International Journal of Pharmaceutics, Manufacturing Performance of Solid Dosage Forms 442 (1-2), 27–34. https://doi.org/10.1016/j. iipharm.2012.09.004.
- Liu, J., Cetinkaya, C., 2010. Mechanical and geometric property characterization of dry-coated tablets with contact ultrasonic techniques. Int. J. Pharm. 392 (1-2), 148–155. https://doi.org/10.1016/j.ijpharm.2010.03.060.
- Molokhia, A.M., Al-Shora, H.I., Hammad, A.A., 1987. Aging of tablets prepared by direct compression of bases with different moisture content. Drug Dev. Ind. Pharm. 13 (9-11), 1933–1946.
- Pitt, K.G., Heasley, M.G., 2013. Determination of the tensile strength of elongated tablets. Powder Technol. 238, 169–175.
- Rantanen, J., Khinast, J., 2015. The Future of Pharmaceutical Manufacturing Sciences. J. Pharm. Sci. 104 (11), 3612–3638. https://doi.org/10.1002/jps.24594.
- Razavi, S.M., Callegari, G., Drazer, G., Cuitino, A.M., 2016. Toward predicting tensile strength of pharmaceutical tablets by ultrasound measurement in continuous manufacturing. Int. J. Pharm. 507 (1-2), 83–89. https://doi.org/10.1016/j. iipharm.2016.04.064.
- Shang, C., Sinka, I.C., Jayaraman, B., Pan, J., 2013. Break force and tensile strength relationships for curved faced tablets subject to diametrical compression. Int. J. Pharm. 442 (1-2), 57–64. https://doi.org/10.1016/j.ijpharm.2012.09.005.
- Simonaho, S.-P., Takala, T.A., Kuosmanen, M., Ketolainen, J., 2011. Ultrasound transmission measurements for tensile strength evaluation of tablets. Int. J. Pharm. 409 (1-2), 104–110. https://doi.org/10.1016/j.ijpharm.2011.02.033.
- Varghese, I., Cetinkaya, C., 2007. Noncontact Photo-Acoustic Defect Detection in Drug Tablets. J. Pharm. Sci. 96 (8), 2125–2133. https://doi.org/10.1002/jps.20838.
- Yoshinari, T., Forbes, R.T., York, P., Kawashima, Y., 2003. The improved compaction properties of mannitol after a moisture-induced polymorphic transition. Int. J. Pharm. 258, 121–131. https://doi.org/10.1016/S0378-5173(03)00157-1.